Annular two-phase flow in a small diameter tube

OpenFOAM simulations with turbulence damping vs optical measurements

Zanetti, Emanuele; Berto, Arianna; Bortolin, Stefano; Magnini, Mirco; Del Col, Davide

DOI
10.1016/j.ijft.2024.100871

Publication date
2024

Document Version
Final published version

Published in
International Journal of Thermofluids

International Journal of Thermofluids 24 (2024) 100871

Contents lists available at ScienceDirect

International Journal of Thermofluids

journal homepage: www.sciencedirect.com/journal/international-journal-of-thermofluids

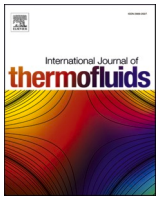

Annular two-phase flow in a small diameter tube: OpenFOAM simulations with turbulence damping vs optical measurements

Emanuele Zanetti [a,b], Arianna Berto [b], Stefano Bortolin [b,*], Mirco Magnini [c], Davide Del Col [b]

[a] Department of Process and Energy, Delft University of Technology, Leeghwaterstraat 39, 2628 CB, Delft, the Netherlands
[b] Department of Industrial Engineering, University of Padova, Via Venezia 1, 35131, Padova, Italy
[c] Department of Mechanical, Materials and Manufacturing Engineering, University of Nottingham, Nottingham, UK

ARTICLE INFO

Keywords:
Annular flow
Numerical simulations
Turbulence damping
VOF method
Liquid film thickness
Adaptive mesh refinement

ABSTRACT

In this work, numerical simulations are performed to predict two-phase annular flow of refrigerant R245fa inside a 3.4 mm diameter vertical channel. The VOF (Volume of Fluid) method implemented in an OpenFOAM solver is used to accurately track the vapor-liquid interface. A 2D axisymmetric domain is considered and the Adaptive Mesh Refinement (AMR) method is applied to the cells near the liquid/vapor interface. The Reynolds-Averaged Navier Stokes (RANS) equations are solved and the *k-ω* SST model is adopted for turbulence modelling in both the liquid and vapor phase. Simulations are used to calculate instantaneous and mean values of the liquid film thickness at mass flux $G = 100$ kg m^{-2} s^{-1} and vapor quality ranging between 0.2 and 0.85. Numerical results are compared against measurements of the liquid film thickness taken during vertical annular downflow. Previous works from the literature and the deviations observed between present numerical and experimental results suggest the need for turbulence damping at the vapor-liquid interface by adding a source term in the ω equation. The simulations show that a low value of the turbulence damping parameter (e.g. 1) causes the average liquid film thickness to increase by 25 %–52 % compared to the non-damped scenario. The interface presents large amplitude disturbance waves in the non-damped case, whereas small ripple waves are predicted when turbulence damping is introduced. Furthermore, the difference between the application of a symmetric and asymmetric treatment for the source term is analysed. From the comparison between experimental data and numerical simulations, it emerges that the value of the correct damping source term to be applied is strictly dependent on the vapor quality.

1. Introduction

Nowadays the design of two-phase (liquid-vapor) flow devices (e.g. condensers and evaporators) is still based on the availability of semi-empirical correlations, whose development and assessment require to carry out wide and often time-consuming experimental campaigns. In the next future, the ever-increasing availability of computational resources together with the development of robust and validated Computational Fluid Dynamics (CFD) codes are expected to promote the use of simulation tools in the two-phase heat transfer sector leading to fast design of devices and to a deeper understanding of the phenomena involved. Among the two-phase flow regimes expected inside channels, one of the most frequently encountered is the annular flow, which is characterized by the presence of a liquid film at the wall and a continuous gas core in the center of the channel [1].

In the past years, some experimental investigations were performed to study the dynamics of the liquid film and to characterize the waves developing at the liquid-gas interface during annular flow. The first studies mainly addressed the creation and development of waves for air-liquid two-phase flows inside large diameter tubes (inner diameter higher than 10 mm) [2–5]. The occurring waves were generally classified in two groups: 1) “disturbance waves”, which display high amplitude and are expected to play a key role in the mass, momentum and energy transfer, and 2) “ripple waves”, having shorter lifetime and smaller height [6–8]. When considering small diameter channels (below 3–4 mm), the measurement of the liquid film thickness (LFT) and the characterization of waves in annular regime are even more complicated as the liquid film is generally thin (about 10-100 μm). To the authors’ knowledge, only a few works are available in the literature on this topic. Donniacuo et al. [9] developed an optical method based on an image processing technique to measure accurately the top and bottom LFT during two-phase annular flow of R245fa in a horizontal 2.95 mm diameter minichannel. Berto et al. [10–12] performed LFT

* Corresponding author.

https://doi.org/10.1016/j.ijft.2024.100871

Available online 19 September 2024

Nomenclature

Δy_s	Turbulent damping length scale [m]
A	Channel section [m^2]
B	Damping parameter [-]
CD	ω Cross diffusion [kg m^{-1} s^{-3}]
$\boldsymbol{f}$	Force [N m^{-3}]
F_1	Blending function [-]
G	Mass flux [kg m^{-2} s^{-1}]
$\boldsymbol{g}$	Gravitational acceleration [m s^{-2}]
H	Heaviside function
k	Turbulent kinetic energy [m^2 s^{-2}]
K	Velocity ratio [-]
L	Channel length [m]
LFT	Liquid film thickness [m]
M	Number of samplings [-]
$\dot{m}$	Mass flow rate [kg s^{-1}]
$\boldsymbol{n}$	Interface normal versor [-]
p	Pressure [Pa]
P	ω Production [kg m^{-1} s^{-3}]
R	Channel radius [m]
r	Radial position [m]
S_ω	ω Source term [kg m^{-3} s^{-2}]
T	Time interval [s]
$\boldsymbol{u}$	Velocity [m s^{-1}]
u	Velocity in the axial direction [m s^{-1}]
V	Volume [m^3]
x	Vapor quality [-] - axial coordinate [m]

Greek letters

α	Volume fraction [-]
β	Turbulence model constant [-]
γ	Turbulence model constant [-]
δ_S	Surface Dirac δ-function [m^{-1}]
δ_t	Turbulence damping asymmetry factor [-]
ε	Void fraction [-]
κ	Interface curvature [m^{-1}]
μ	Dynamic viscosity [Pa s]
ν	Kinematic viscosity [m^2 s^{-1}]
ρ	Density [kg m^{-3}]
σ	Surface tension [N m^{-1}]
$\sigma_{\omega 1}$	Turbulence model constant [-]
τ	Time [s]
ω	Specific rate of dissipation [s^{-1}]

Subscripts

0	Inlet section
b	Base
int	Interface
j	Longitudinal position
l	Liquid
low	Lower limit
m	Mean
t	Turbulent/eddy
up	Upper limit
v	Vapor
σ	Surface tension

measurements with refrigerants R245fa, R134a and HFE7000 inside a 3.4 mm inner diameter channel by means of shadowgraph technique and chromatic confocal imaging. The liquid film thickness was found to be highly influenced by the vapor density and the liquid viscosity of the tested fluids. Zhang et al. [13] measured the LFT for flow condensation of R245fa and zeotropic mixtures of R134a/R245fa in a circular 1 mm diameter microchannel using a laser focus displacement meter. The average LFT resulting from the measures was in turn used to develop a prediction method for LFT during annular flow in microchannels. A wide experimental database on LFT values encompassing different operating conditions and channel diameters is still needed for understanding the involved mechanisms and for the validation of CFD simulations.

Regarding the numerical simulations, the number of works focusing on annular flow regime is rather limited and this is due to the fact that CFD tools still require a vast amount of computational resources to be able to properly track the complex liquid-gas interface behavior [14]. In an early work by Kishore and Jayanti [15], a simplified model for simulating steady-state annular flow was proposed. In their model, the gas phase was solved separately considering the interface to behave like a rough wall and using modified properties to account for entrained droplets, whereas the liquid film was treated separately using empirical correlations to determine its flow rate. Han and Gabriel [16] employed the Volume of Fluid (VOF) method to study the interfacial waves in air-water annular flow. Their work focused on a 2D vertical upward co-current configuration within a 9.525 mm internal diameter tube. The numerical simulations revealed that the disturbance waves were notably less irregular and chaotic compared to experimental visualizations. In the work of Guo et al. [17], the VOF method was used to study the stability of the interface in a laminar, incompressible annular flow inside a small diameter channel (2 mm). Their model was then used to perform simulations of annular-flow boiling [18]. They obtained reasonably good agreement with existing correlations and found that a pure conductive thermal model applied to the simulated liquid film greatly underestimates the heat transfer coefficient. Core-annular flow, in which the fluids (oil and water) have similar density but different viscosity has been recently simulated [19,20]. Simulations were conducted in an axisymmetric domain using the *k-ε* model and compared against results obtained by run direct numerical simulation (DNS). Even though good predictions in terms of friction factor were obtained by the simulations, it was observed that there is a strong dependence between the waves thickness probability and the domain length: a reduced domain length manages to get a less broad wavelength spectrum.

When simulating annular flow, both the liquid and the vapor phases can be in the turbulent regime and the Reynolds Averaged Navier Stokes (RANS) equations are usually solved [21,22] since they offer the possibility to reduce the numerical cost of the simulations. However, RANS-based approaches display problems in handling turbulence near the liquid-gas interface: according to DNS [23], the gas-liquid interface is found to behave similarly to a solid wall in single-phase flow and this is not accounted for in the common RANS models. For this reason, with reference to the *k-ω* SST model by Menter [25], an empirical turbulence damping approach was developed by Egorov [24], which added a source term in the ω equation near the interface. The source term was formulated in analogy with the boundary conditions for ω near a solid wall in the original k-*ω* SST model by Menter [25], thus effectively modeling the interface as a solid wall, with a magnitude proportional to a non-dimensional coefficient originally set to 10 in Menter [25] and 100 in Egorov [24]. The model was recently reviewed and modified by Fan and Anglart [26] who introduced the possibility to treat asymmetrically the damping source in the two phases. Their reference experimental benchmark consisted of a rectangular 10 × 20 cm channel vertically oriented with air-water flowing downward [27]. Simulations were run for inlet water velocity equal to 3 m s^{-1} and inlet air velocity ranging between 45.4 and 118.7 m s^{-1}. Both in the original and in the updated version of the damping model, the source term is mesh-dependent and no indication about the value to be adopted for the turbulence damping is found in the open literature. For instance, in their rectangular configuration, Fan and Anglart [26] varied its value between 0 and

1000. Porombka and Höhne [28] used the Egorov model to simulate counter-current stratified flow of air-water in a horizontal 9 mm square channel with inlet water velocity equal to 0.7 m s^{-1} and gas inlet velocity equal to 4.44 m s^{-1}. In their numerical setup, a value of the damping parameter equal to 100 was used. Gada et al. [30] applied a similar damping procedure in 3D simulations of air-water stratified flow in a horizontal 6 mm circular pipe with fixed air velocity of 3 m s^{-1} and four water velocities between 0.12 and 0.319 m s^{-1}. With a damping parameter set to 500, they obtained an improvement in the prediction of pressure drop as compared to the case without damping, but concluded that the damping requires further modeling. Varallo et al. [21] recently performed numerical simulations of downward air-water annular flow in a 32.4 mm diameter circular channel using ANSYS Fluent: in their study, both 3D and 2D simulations were realized for liquid Reynolds number equal to 1250 and gas Reynolds number equal to 25000 and 30000; a damping parameter equal to 100 was used. Their error in the prediction of the mean liquid thickness was found to be lower than 10 % however, they concluded that more conditions should be explored and that a systematic study on the damping parameter is needed. Fan et al. [14] simulated downward annular flow with OpenFOAM software. The modified damping model [26] was also implemented in their 3D simulations to test different values of the damping parameter on the main flow characteristics [31]. Their numerical setup consisted of a circular channel vertically oriented with 11.7 mm internal diameter. The simulations were realized at liquid Reynolds number equal to 350 and inlet gas velocity equal to 18 m s^{-1}, while the damping parameter was varied in a range between -10 and 50, considering both a symmetric and asymmetric treatment of the source term. They evaluated the mean and modal values of liquid film thickness, waves amplitude, velocity, longitudinal size and frequency as a function of the downstream position. The best agreement with the experiments was obtained using a damping parameter equal to 20 (both axisymmetric and symmetric treatment). In addition, while the frequency of disturbance waves was overestimated, the frequency of ripple waves was underestimated by the model. They concluded that validation is needed for other experimental conditions.

From the literature analysis it emerges that there are still significant open questions on the effect of turbulence near the interface during vapor-liquid annular flow. The aim of this work is to systematically investigate the effect of turbulence damping on the liquid film thickness by performing annular flow CFD simulations and comparing the numerical results against experimental data. The main novelties of the paper can be summarized in the following points:

- An OpenFOAM solver based on the VOF method is used to perform transient simulations with refrigerant R245fa flowing inside a small diameter (3.4 mm) circular channel at mass flux equal to 100 kg m^{-2} s^{-1} and vapor quality ranging between 20 % and 77 %.
- Adaptive Mesh Refinement (AMR) is applied at the liquid/vapor interface.
- The Reynolds-Averaged Navier Stokes (RANS) equations are solved and the *k-ω* SST model is adopted in both the liquid and vapor phase. A turbulence damping method [26] is used to damp the turbulence at the interface by adding a symmetric or asymmetric source term to the ω equation.
- The numerical results are compared against experimental data both in terms of average liquid film thickness values and instantaneous liquid film thickness values sampled at 1000 Hz frequency.

The results here presented find also potential applications in CFD simulations of condensation heat transfer inside small diameter channels. Condensation heat transfer is encountered in heat pump and refrigeration systems. During in-tube condensation, annular flow is a recurrent flow pattern and the main thermal resistance is associated to the liquid film. Adiabatic numerical simulations capable to track the vapor-liquid interface represents the first step for the development of CFD codes for the prediction of phase-change processes.

2. Numerical simulations

2.1. Governing Equations

Annular flow is modeled using the so-called "one fluid" formulation, meaning that a single set of governing equations is used to describe the whole two-phase system [32]. Under the assumptions of Newtonian incompressible fluid and adiabatic conditions, the continuity (Eq. (2.1)) and momentum (Eq. (2.2)) equations can be written as follows:

$$\frac{\partial \rho}{\partial \tau} + \nabla \cdot (\rho \boldsymbol{u}) = 0 \tag{2.1}$$

$$\frac{\partial (\rho \boldsymbol{u})}{\partial \tau} + \nabla \cdot (\rho \boldsymbol{u}\boldsymbol{u}) = -\nabla p + \nabla \cdot \left[(\mu + \mu_t)\left(\nabla \boldsymbol{u} + \nabla \boldsymbol{u}^T\right)\right] + \rho \boldsymbol{g} + \boldsymbol{f_\sigma} \tag{2.2}$$

Where ρ is the fluid density, μ is the dynamic viscosity, μ_t is the eddy viscosity, τ is the time, p is the pressure, $\boldsymbol{g}$ is the gravitational acceleration and $\boldsymbol{u}$ is the velocity. Eq. (2.2) accounts for the presence of an interface, located in a generic position $\boldsymbol{x_{int}}$, through the surface tension force term $\boldsymbol{f_\sigma}$:

$$\boldsymbol{f_\sigma} = \sigma \kappa \boldsymbol{n} \delta_S \tag{2.3}$$

Where σ is the surface tension, κ is the interface curvature and $\boldsymbol{n}$ is the versor normal to the interface. In Eq. (2.3) δ_S is a surface Dirac delta-function which is non-zero only at the interface and ensures that surface tension is applied only to interfacial cells, as in the Continuum Surface Force method [33].

The Volume of Fluid (VOF) method is used to reconstruct and advect the interface. The VOF method is based on the use of a color function (or volume fraction) α, which is an approximation of the Heaviside function for a discretized domain. For a generic volume V, the color function can be defined as:

$$\alpha = \frac{1}{V}\int_V H \, \mathrm{dV} \tag{2.4}$$

Therefore, the color function α is a scalar field, which can assume values between 0 and 1 in each discretized cell depending on the amount of liquid and vapor. In this work the Heaviside function H is 1 in the liquid phase and thus $\alpha = 1$ in the liquid, $\alpha = 0$ in the vapor, and $0<\alpha<1$ in an interface cell.

In order to solve the discretized equations (continuity and momentum), an additional transport equation related to the advection of the volume fraction scalar field must be solved:

$$\frac{\partial \alpha}{\partial \tau} + \nabla \cdot (\alpha \boldsymbol{u}) = 0 \tag{2.5}$$

Following the one fluid formulation, the density and the dynamic viscosity can be expressed as a function of the color function:

$$\rho = \rho_l \alpha + \rho_v (1 - \alpha) \tag{2.6}$$

$$\mu = \mu_l \alpha + \mu_v (1 - \alpha) \tag{2.7}$$

Where the subscripts l and v refer to the liquid and the vapor phase, respectively.

Finally, the interface normal vector $\boldsymbol{n}$ and the curvature can be defined as:

$$\boldsymbol{n} = \frac{\nabla \alpha}{|\nabla \alpha|} \tag{2.8}$$

$$\kappa = -\nabla \cdot \boldsymbol{n} \tag{2.9}$$

2.2. Numerical setup and boundary conditions

Numerical simulations of annular downward flow in a circular cross-section channel have been performed considering a 2D axisymmetric

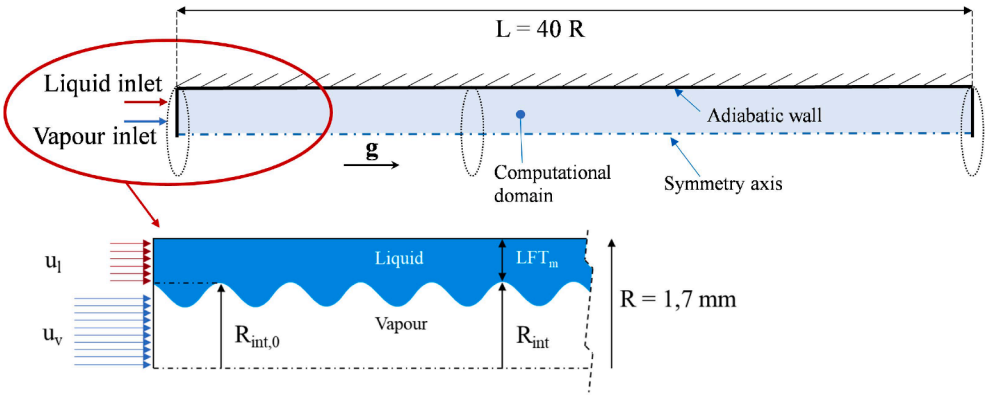

Fig. 1. Numerical setup used for simulation of annular downward flow (axisymmetric domain). The boundary conditions, the liquid film thickness (LFT) and the radius R_{int} at the vapor-liquid interface are shown.

computational domain. This approach is not new for annular flow simulations [16–18] and this configuration has been adopted to reduce the computational cost. The simulation setup is displayed in Fig. 1. The channel radius R is equal to 1.7 mm to match the conditions of the experimental tests [10,34]. For the computational domain, a higher channel length L, equal to 40R, has been adopted to guarantee the development of the two-phase fluid flow (see Section 3.2).

The simulations have been realized at different values of total mass flux G and vapor quality x of the fluid R245fa, which are considered input parameters in the numerical model, and are thus utilised to set velocity and volume fraction boundary conditions at the channel inlet as explained below. Considering that annular flow is not a steady-state process, the mass flux G for a generic circular cross-section can be defined as:

$$G = \frac{\dot{m}}{A} = \frac{2}{R^2}\frac{1}{T}\int_0^T\int_0^R \rho u r \, dr d\tau \tag{2.10}$$

Where $\dot{m}$ is the refrigerant mass flow rate, u is the axial velocity and A is the channel cross-section.

The vapor quality x is defined as the ratio between the total mass of vapor to the total mass of fluid that flows across a generic cross-section of the channel in a selected time interval T:

$$x = \frac{\int_0^T \dot{m}_v \, d\tau}{\int_0^T \dot{m} \, d\tau} \tag{2.11}$$

where:

$$\dot{m}_v = 2\pi\frac{1}{T}\int_0^T\int_0^R (1-\alpha)\rho u r \, dr d\tau \tag{2.12}$$

The inlet boundary conditions required by the solver are the axial velocity and volume fraction, but they cannot be directly derived from Eq. (2.10) and Eq. (2.12).

To simplify the determination of the boundary conditions at the inlet cross-section, the following assumptions are made:

- only two regions exist in the inlet cross-section, one occupied by the liquid and one occupied by the vapor;
- the liquid enters the domain in contact with the wall and the vapor enters in the channel core;
- the axial velocities of the liquid and vapor phase at the inlet (namely u_l and u_v) are uniform and constant with time, as depicted in Fig. 1.

Eq. (2.10) and Eq. (2.11) can thus be rewritten as follows for the inlet section:

$$G = \frac{\pi\left[\left(R^2 - R_{int,0}^2\right)\rho_l u_l + R_{int,0}^2 \rho_v u_v\right]}{\pi R^2} \tag{2.13}$$

$$x = \frac{R_{int,0}^2 \rho_v u_v}{R^2\rho_v u_v + \left(R^2 - R_{int,0}^2\right)\rho_l u_l} \tag{2.14}$$

In Eq. (2.13) and Eq. (2.14) $R_{int,0}$ is the radius of the interface at the channel inlet (i.e. the radial distance between the symmetry axis and the interface).

Concluding, we have now two equations, Eq. (2.13) and Eq. (2.14), with three unknowns, i.e., the two velocities plus the position of the interface at the inlet. The inlet boundary conditions can be obtained by adding a further constraint. In the present study, we decided to fix the ratio between the vapor and liquid velocity phase (K). A discussion about this hypothesis is reported in Section 3.2.

At the channel wall, a no-slip condition for velocity is set. The liquid is assumed to wet the wall (α=1 boundary condition at the wall) according to the experimental tests [10]. With reference to Eq. (2.2), the Boussinesq assumption is used and a value for the eddy viscosity μ_t is calculated with a specific turbulence model. The k-ω model is adopted in the present work, given its success in simulating annular flows [14,21] and stratified/annular flow of refrigerants during condensation [35], and the possibility to directly integrate the turbulence damping effect into the equations, as explained below. In addition, the blending functions introduced in the SST version of k-ω model guarantee the robustness of the standard k-ω model in the near-wall region and that of the $k\varepsilon$ model far from the boundary layer. In the model, two transport equations for the turbulent kinetic energy k and the specific rate of dissipation ω are solved. In particular, the transport equation for ω can be written as follows:

$$\frac{\partial(\rho\omega)}{\partial\tau} + \nabla\cdot(\rho\boldsymbol{u}\omega) = \nabla\cdot\left[\left(\mu + \frac{\mu_t}{\sigma_{\omega 1}}\right)\nabla\omega\right] + \left(\gamma\frac{\rho}{\mu_t}\right)P + (1-F_1)\mathrm{CD} - \rho\beta\omega^2 + S_\omega \tag{2.15}$$

where $\sigma_{\omega 1}$, γ and β are model constants that take the same values as in Menter [25], F_1 is a blending function, P and CD represent the production and the cross-diffusion term, respectively. Furthermore, in Eq. (2.15), $\rho\beta\omega^2$ is the dissipation term and S_ω is the source term that forces the turbulence damping at the interface. The S_ω term has been modeled according to Egorov [24], with the modifications proposed by Fan and Anglart [26]:

$$S_\omega = 2|\nabla\alpha|\beta\Delta y_s\left(\frac{6}{\beta\Delta y_s^2}\right)^2 B^2\left(\delta_t\frac{\alpha\mu_l^2}{\rho_l} + \frac{(1-\alpha)\mu_v^2}{\rho_v}\right) \tag{2.16}$$

In Eq. (2.16) the terms in brackets have the same shape of the hyperbolic solution of ω usually adopted for the viscous sublayer [36],

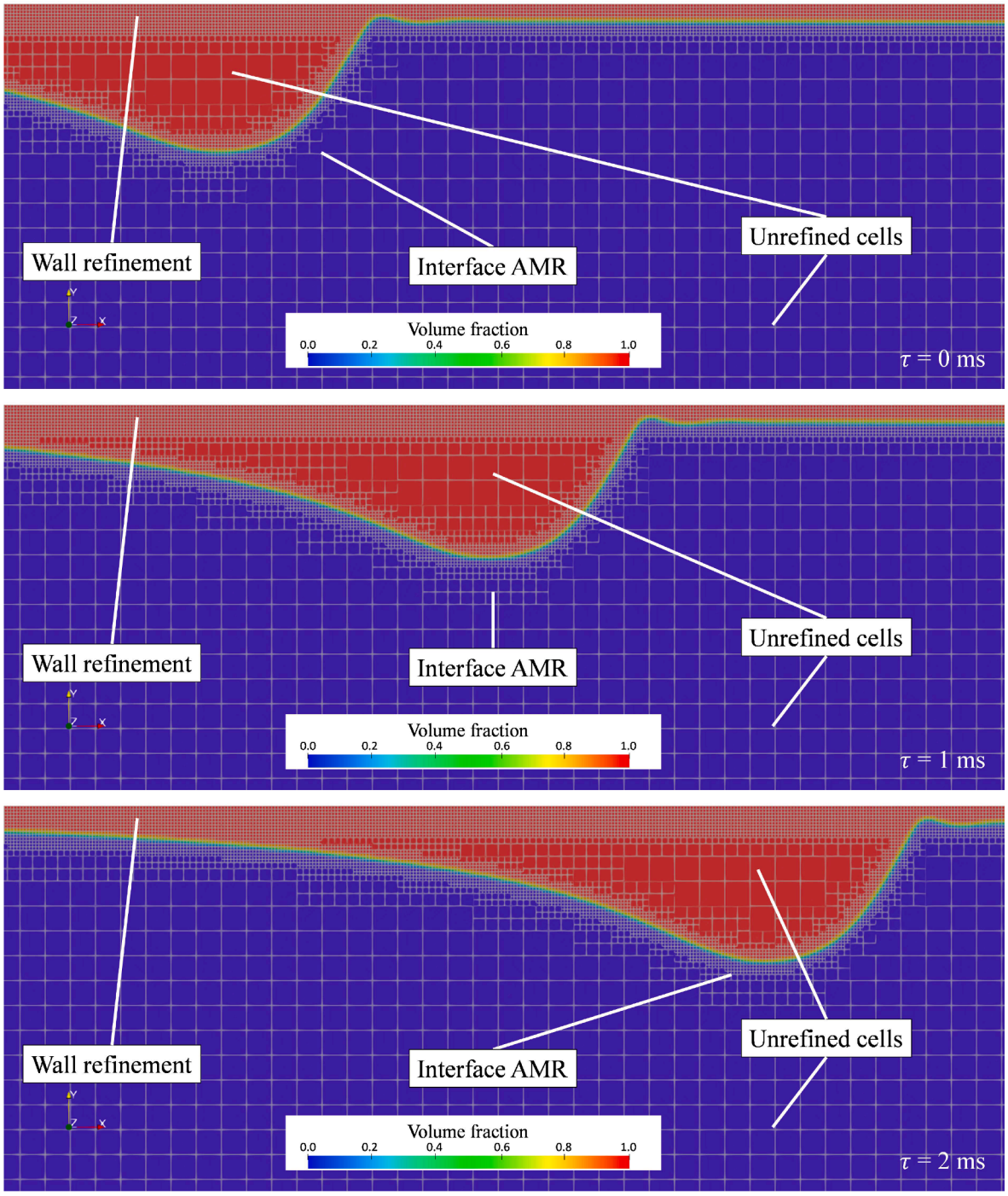

Fig. 2. Mesh size variations in the computational domain at three different time steps during the passage of a liquid wave. Unrefined cells in the liquid/vapor, refined cells with AMR at the interface (2 levels of refinement), and a layer of refined cells at the wall (3 levels of refinement) can be identified.

with the difference that the contributions given by the liquid and vapor phase are considered separately. In addition, the term $2|\nabla\alpha|$ arises from the definition of surface area density (equal to $\alpha \bullet 2\nabla\alpha$ for the liquid and $(1\text{-}\alpha)\bullet 2\nabla\alpha$ for the vapor) and has the function of activating the source term at the liquid/vapor interface only. Δy_s is the turbulence damping length scale and it has been determined according to [26], whose formulation guarantees the source term to be independent from the mesh resolution in the direction tangential to the interface. The parameter δ_t defines the symmetric/asymmetric treatment of turbulence damping and was introduced by [26], who suggested to set it to:

$$\delta_t = -\frac{\mu_v^2}{\mu_l^2}\frac{\rho_l}{\rho_v} \tag{2.17}$$

When the properties of liquid and vapor become similar (thus approaching a single-phase problem) the damping goes to zero. This method applies an asymmetric formulation of the damping, because the minus sign in Eq. (2.17) induces an increase of turbulence in the liquid (reduction of the ω source), in contrast to the damping effect which, on the contrary, only occurs in the vapor. The impact of this asymmetric treatment and a comparison with a symmetric damping approach will be discussed in Section 5.3. Finally, in Eq. (2.16), B is the turbulence

Table 1
List of mesh configurations for the sensitivity analysis. Simulations have been run with R245fa at mass flux equal to 100 kg m^{-2} s^{-1} and vapor quality equal to 0.77.

Case	Unrefined cell size	Number of refinements at wall cells	Number of refinements at interface cells	Wall cell size	Interface cell size
1	*R*/16	2	2	*R*/64	*R*/64
2	*R*/16	3	3	*R*/128	*R*/128
3	*R*/16	4	3	*R*/256	*R*/128
4	*R*/32	2	2	*R*/128	*R*/128
5	*R*/32	3	3	*R*/256	*R*/256
6	*R*/32	4	3	*R*/512	*R*/256
7	*R*/64	1	1	*R*/128	*R*/128
8	*R*/64	2	2	*R*/256	*R*/256

damping parameter, which is usually considered to be mesh and case-dependent [31].

All the presented simulations have been run in OpenFOAM environment, using a customized solver created starting from the built-in solver interIsoFoam by adding the libraries related to the turbulence damping and adaptive mesh refinement. In the solver, pressure-velocity coupling is performed with the PIMPLE algorithm, which is a combination of the SIMPLE and PISO algorithms. Regarding the volume fraction equation (Eq. (2.5)), the reconstruction/advection steps are made according to the geometrical VOF method proposed by Roenby et al [37]. All flow equations except for volume fraction advection are discretized in time with a fully-implicit scheme. The time step of the simulation is adaptive and set to yield a Courant number of 0.5.

Each simulation is initialized considering the computational domain filled only with the saturated vapor phase. According to the boundary conditions, the liquid is injected into the domain and, as it enters, it progressively advances along the channel forming a continuous film along the wall. After a certain time interval, the two-phase flow close to the exit of the channel can be considered fully developed and data processing is performed (see Section 3.1).

2.3. Mesh design

A structured mesh made of square cells has been considered as the base grid. Near the wall, the cells are recursively refined by splitting each cell into 4 parts, according to the desired number of refinements. These near-wall cells are never unrefined to allow a discretization of the base liquid film in each investigated condition (see Fig. 2 which displays the region close to the wall during the passage of a liquid wave).

Adaptive mesh refinement (AMR) is used during runtime to refine the cells near the interface and accurately track the liquid waves. The volume fraction is used as the parameter for the refinement of the grid at the interface. A cell is divided when:

$$\alpha \in \left[\alpha_{\text{low}}, \alpha_{\text{up}}\right] \tag{2.18}$$

In this work, the lower refinement value of α (α_{low}) was fixed to 0.1 and the upper value (α_{up}) was fixed to 0.9. It must be noted that, in the layer near the wall, AMR is inhibited to avoid excessively small cell sizes. The great advantage of this method is that the aspect ratio of the original cell is maintained. The AMR method has already proven its effectiveness when using VOF-based models: Mehdizadeh et al. [38] stated that they managed to reduce down to 96 % the number of required cells to reproduce slug flow conditions in minichannels. This method has been also recently used by Vermaak et al. [39] for the numerical simulation of evaporation during bubble and slug flow in minichannels. In their simulation, the refinement process was activated every 5 time steps. The same interval was used in the present work.

The resulting mesh is depicted in Fig. 2, where three mesh zones can be identified:

a) unrefined (fixed size) cells in the vapor bulk and in the liquid film (far from the wall);
b) refined (fixed size) cells at the wall that cannot be unrefined;
c) cells that are refined (AMR method) near the vapor-liquid interface.

3. Sensitivity analysis to mesh and inlet conditions

3.1. Mesh sensitivity

A mesh sensitivity analysis has been performed with R245fa, mass flux G equal to 100 kg m^{-2} s^{-1} and at the highest value of vapor quality (x=0.77) considered from the experiments. Increasing the vapor quality leads to thinning the liquid film thickness and therefore this condition is the most critical in terms of number of cells inside the liquid. The total duration of a simulation was set to be equal to 1.5 s: the initial 0.5 s period allows the liquid to reach the end of the channel, the subsequent 0.5 s period is dedicated to flow development and to reach time-averaged steady-state conditions, and the final 0.5 s period is used for data sampling and processing.

According to Fig. 1, the instantaneous liquid film thickness LFT calculated in a certain position j along the channel axis is defined as:

$$\text{LFT}_j = R - R_{\text{int},j} \tag{3.1}$$

The sensitivity analysis has been done considering different mesh configurations and, with reference to the mesh regions defined in Section 2.3, by varying:

a) The size of the unrefined (largest) cells in the vapor/liquid bulk (between *R*/16 and *R*/64).
b) The minimum size of the cells at the wall (between *R*/32 and *R*/512). The thickness of the wall refinement layer is equal to the size of the largest cell.
c) The minimum size of the cells at the liquid-vapor interface (between *R*/32 and *R*/256). A summary of the conditions is reported in Table 1. All the simulations have been run without considering turbulence damping (B=0).

The results are reported in Fig. 3 a) and b) which show the mean liquid film thickness $\text{LFT}_{j,m}$ calculated close to the outlet section (j=x/L=0.9):

$$\text{LFT}_{m,j} = \frac{1}{M}\sum_{0}^{M}\text{LFT}_j \tag{3.2}$$

In Eq. (3.2) M is the number of samplings (sampling time interval 0.001 s). Fig. 3 c) and d) report the results in terms of 'base' liquid film thickness $\text{LFT}_{b,j}$, which is defined as the average thickness of the liquid film, calculated by only considering the M_b values below $\text{LFT}_{m,j}$:

$$\text{LFT}_{b,j} = \frac{1}{M_b}\sum_{0}^{M_b}\text{LFT}_j \left(\text{LFT}_j < \text{LFT}_{m,j}\right) \tag{3.3}$$

For sake of simplicity, the notations LFT_m and LFT_b are used to refer to $\text{LFT}_{m,j}$ and $\text{LFT}_{b,j}$ respectively, considering, unless otherwise indicated, j=0.9. Note that the expressions in Eq. (3.2) and Eq. (3.3) have been used also to process the experimental data used for comparison, so that the same data reduction technique is adopted [10].

It is worth mentioning that the sampling time interval (0.001 s) is different from the time step of the simulations, which is adaptive and depends on both the operative conditions and on the selected value for the Courant number (see Section 2.2). The simulation time step was

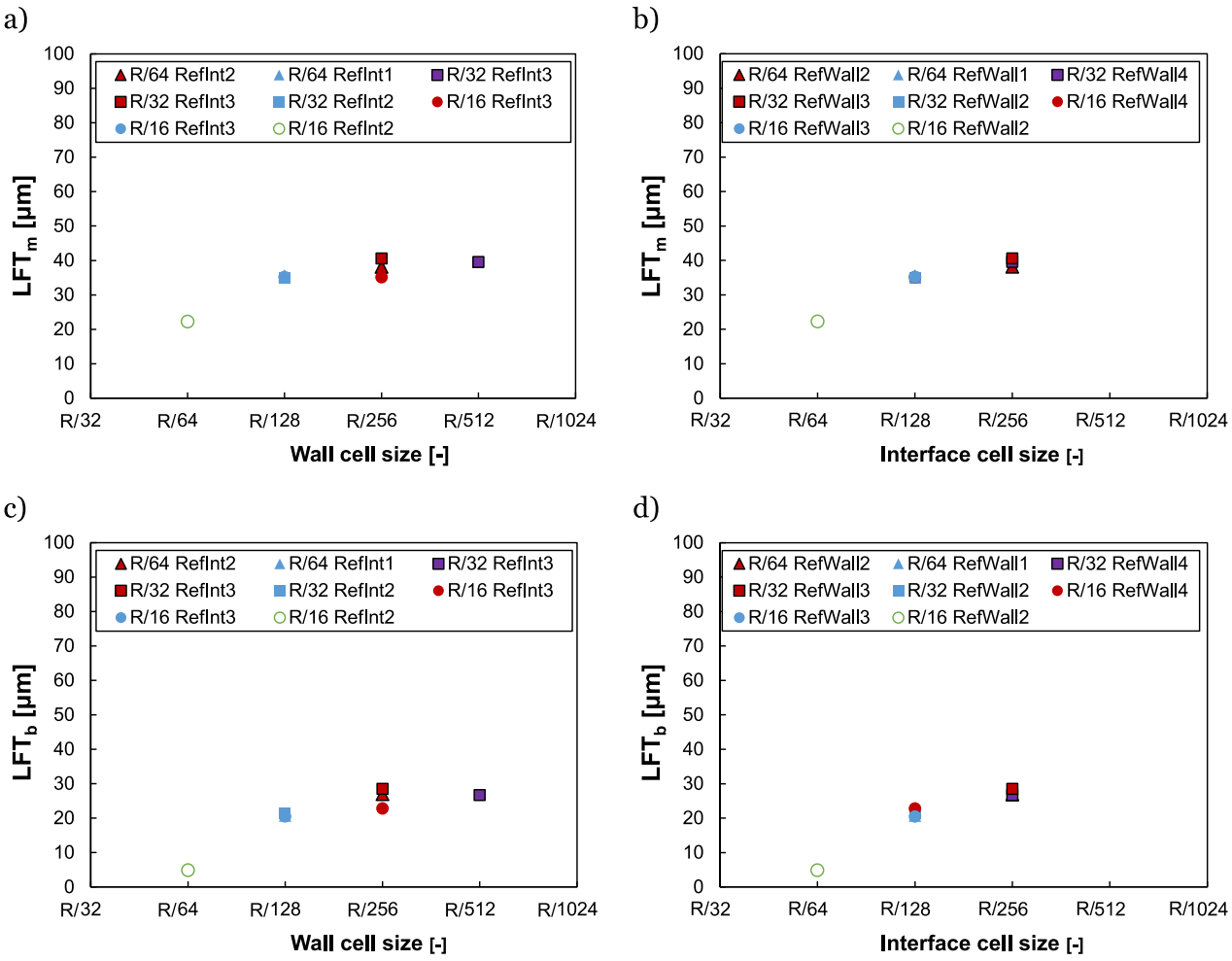

Fig. 3. Mean (LFT_m) and base (LFT_b) liquid film thickness computed for the different mesh configurations of Table 1 vs the minimum size of the cells at the wall (a, c) and vs the minimum cell size at the interface (b, d). Colors represent the minimum cell size at the wall ($R/64$ green, $R/128$ blue, $R/256$ red and $R/512$ violet). Dots style identifies the minimum size of the cells at the interface ($R/64$ void, $R/128$ full, $R/256$ full with border). Dots shape identifies the size of the unrefined cells ($R/16$ circle, $R/32$ square, $R/64$ triangle). Simulations have been realized with R245fa at mass flux equal to 100 kg m^{-2} s^{-1} and vapor quality equal to 0.77.

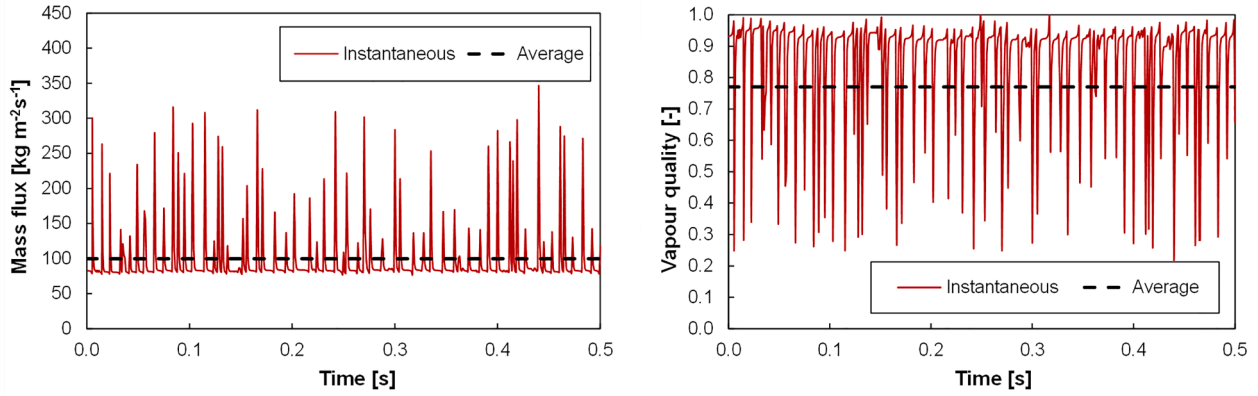

Fig. 4. Instantaneous and time-average values of the mass flux and vapor quality evaluated at x/L=0.9. Conditions are: fluid R245fa, mass flux equal to 100 kg m^{-2} s^{-1} and vapor quality equal to 0.77.

found to vary between 10^{-6} and 10^{-7} s for the presented simulations.

Fig. 3 a) reports the computed mean and base liquid film thickness as a function of the minimum cell size at the wall. In the legend, the size of the unrefined cells and the number of refinement levels applied at the interface are also reported for all the considered configurations. A decrease in the minimum size of the cells at the wall from $R/64$ (26.6 µm) to $R/128$ (13.3 µm) results in an increase in the liquid film thickness. However, when the minimum cell size at the wall is equal to $R/256$ (6.6 µm), the value of the average liquid film thickness is 40.6 µm (three refinement levels at the interface, size of unrefined cells equal to $R/32$) and, for a minimum cell size at the wall equal to $R/512$ (3.3 µm), the computed LFT_m is 39.6 µm (three refinement levels at the interface, size

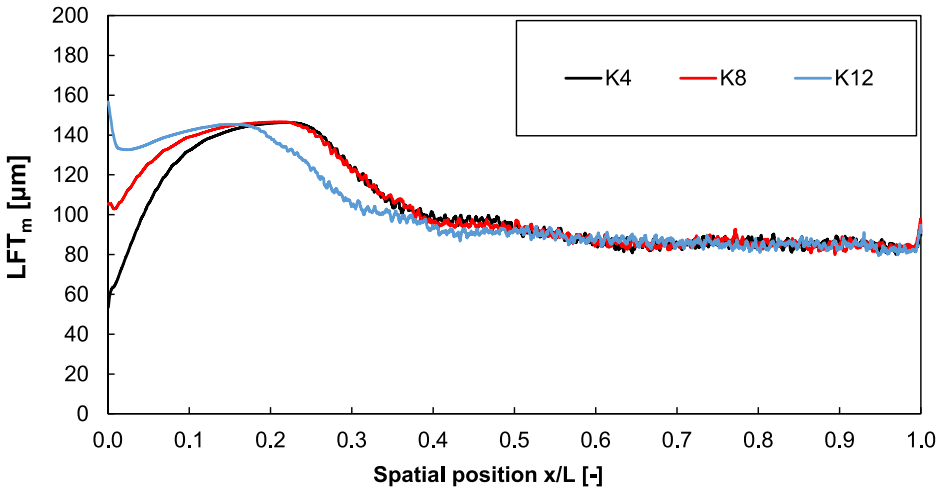

Fig. 5. Computed time-averaged liquid film thickness along the channel assuming different values for the velocity ratio ($K=u_v/u_l=$ 4, 8, 12). Simulations have been run with R245fa at mass flux equal to 100 kg m^{-2} s^{-1} and vapor quality equal to 0.39.

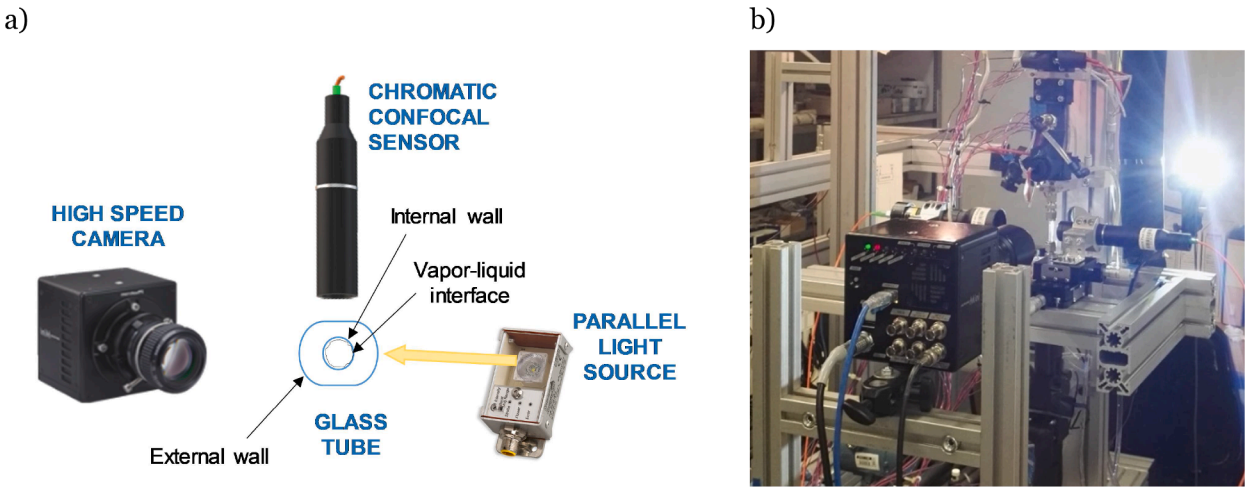

Fig. 6. Sketch (a) and picture (b) of the optical setup for liquid film thickness measurements used in Berto et al. [10,11], consisting of a high-speed camera, a LED, a glass tube and chromatic confocal sensor.

of unrefined cells equal to $R/32$), meaning that from $R/256$ the results can be considered mesh independent. Fig. 3 b) depicts the mean LFT as a function of the minimum size of the cells at the interface. In the legend, the size of the unrefined cells and the number of refinement levels applied at the wall are also reported for all the tested configurations. Fig. 3 b) shows that, independently of the size of the unrefined cells at the wall, the liquid film thickness tends to assume the same values for a fixed size of cells at the interface. An increasing trend of the liquid film thickness is observed with the interface cell size, with an asymptotic value reached when this is equal to $R/256$. The same conclusions can be inferred for the base film thickness, which is reported as a function of both the wall cell size and interface cell size in Fig. 3 c) and d). Among the possible configurations reaching the same asymptotic value in Fig. 3 b) and d), a mesh with unrefined cell size equal to $R/32$ and 3 refinement levels at the wall and at the interface ($R/256$) has been used for the simulations. These cells size correspond to 53 μm in the unrefined regions and 6.6 μm in the finest regions (near-wall and interface).

For the calculation of the liquid film thickness in Eq. (3.2), M is set equal to 500, corresponding to the last 0.5 s of the simulated time interval. It has been checked that a time interval equal to 0.5 s was sufficiently large to obtain constant values for the main time-averaged quantities (eg. LFT, void fraction) characterizing the wavy annular flow. Fig. 4 reports the instantaneous values of mass flux and vapor quality at the j=0.9 cross-section together with the corresponding time-averaged values (straight dotted lines), calculated according to Eq. (2.11) and Eq. (2.13). It can be observed that the average values of mass flux and vapor quality match the boundary conditions (G=100 kg m^{-2}s^{-1} and vapor quality x=0.77). The same results have been obtained for all the tested operative conditions.

3.2. Effect of the inlet boundary conditions

As reported in Sec 2.2, to set the inlet boundary conditions, a guess value for the ratio K between the vapor and liquid velocities must be assumed:

$$K = \frac{u_v}{u_l} \tag{3.4}$$

By solving the system of Eq. (2.14), Eq. (2.15) and Eq. (3.4) it is possible to initialize the axial velocities of liquid and vapor phases (u_l and u_v) and the interface radius $R_{int,0}$ at the inlet of the channel.

The effect of the guess value for K has been investigated. In Fig. 5, the time-averaged values of liquid film thickness (LFT$_m$) along the longitudinal direction ($0<j<1$) for three velocity ratios (K = 4, 8, 12) are reported. The mass flux G is equal to 100 kg m^{-2}s^{-1} and the vapor quality x is equal to 39 %. It can be observed that at the inlet section, LFT$_m$

Table 2
Experimental and computed values of liquid film thickness (LFT) and void fraction ε for R245fa at mass flux equal to 100 kg m^{-2} s^{-1} and 40 °C saturation temperature. The experimental expanded uncertainty (coverage factor equal to 2) calculated as indicated in Berto et al. [10] is also reported within brackets.

	Experimental			Numerical			
Vapor quality	LFT_m [μm]	LFT_b [μm]	ε [%]	B	LFT_m [μm]	LFT_b [μm]	ε [%]
0.20	161 (±15)	97 (±5)	82.0%	0	125	72	85.8%
				0.025	129	76	85.4%
				0.1	153	102	82.8%
				0.25	154	118	82.7%
				1	157	125	82.4%
				10	161	122	82.0%
0.39	103 (±10)	67 (±4)	88.3%	0	83	47	90.5%
				0.025	83	52	90.5%
				0.1	96	57	89.0%
				0.25	114	78	87.1%
				1	123	98	86.1%
				10	118	90	86.6%
				100	106	74	87.9%
				1000	100	71	88.6%
0.58	66 (±10)	44 (±4)	92.4%	0	58	37	93.3%
				0.1	61	39	92.9%
				0.25	69	44	92.0%
				1	88	64	89.9%
				10	66	50	92.3%
				100	58	42	93.3%
0.77	58 (±7)	38 (±4)	93.3%	0	41	29	95.2%
				0.1	41	30	95.3%
				1	55	36	93.6%
				10	57	40	93.4%
				100	49	35	94.3%
				1000	50	35	94.2%

increases with the ratio K. However, after the axial position x/L=0.6, an asymptotical value, between 80 μm and 86 μm, is reached: the developed flow structure is found to be independent of the initial conditions. This conclusion was also confirmed by an independent test where the velocity profile arising from the analytical solution of the continuity and momentum equations (laminar two-phase annular flow in cylindrical coordinates, free-shear at the interface) is used as input for the simulation. The same asymptotical value of the LFT_m was obtained at the outlet section of the channel.

4. Experimental measurements

The liquid film thickness was measured during R245fa downward annular flow inside an adiabatic glass channel with internal diameter equal to 3.4 mm, as reported in Berto et al. [10,12]. The glass channel is located after a counter-flow tube-in-tube heat exchanger (540 mm long) which is used to control the vapor quality at the inlet to the glass tube. The refrigerant R245fa enters the heat exchanger as superheated vapor and it is partially condensed rejecting heat to the cold water (secondary fluid) that flows on the external annulus. The tube-in-tube heat exchanger is divided into three heat transfer sectors, and after them the liquid-vapour flow enters the glass channel used for film thickness measurement.

Each of the heat transfer sectors is instrumented to allow the evaluation of the exchanged heat flow rate and thus determine the specific enthalpy and the vapour quality at the outlet of each sector. The vapor quality at the exit of the third sector corresponds to the vapor quality at the inlet of the glass window used for film thickness measurements. An uncertainty analysis was performed following the JCGM [40] guidelines. Considering the present experimental database, the maximum expanded uncertainty on the vapor quality (coverage factor equal to 2) was equal to ±0.01. Additional information on the experimental setup and the procedure for data reduction and uncertainty analysis is reported in Azzolin et al. [10,34,41].

As shown in Fig. 6, the optical setup used for performing liquid film thickness measurements consists of a high-speed camera, a LED light source, a borosilicate glass tube, and a chromatic confocal sensor [42]. The borosilicate glass tube (3.4 mm inner diameter) is designed with two symmetric curved parts displaying a special curvature to magnify the liquid film thickness observed by the high-speed camera. The liquid film thickness can be measured using two complementary techniques: the shadowgraph technique, applied to the flow images acquired by the high-speed camera, and the chromatic confocal imaging. RGB images are obtained using a high-speed camera (Photron® FASTCAM Mini UX100), together with a Navitar® Zoom 7000 18–108 mm macro lens and a LED light source. With the shadowgraph technique, the images are first binarized [11]. A ray-tracing method (Médéric et al. [43]) is then applied to link the apparent liquid film thickness obtained by pixel counting to the real one. A chromatic confocal sensor (CL2MG70 sensor pen by STIL®) is used to measure the liquid film thickness at a fixed axial location along the tube with high temporal resolution (1000 Hz). It allows to evaluate film thicknesses up to 300 μm, provided that the slope of the liquid-vapor interface is lower than 28°. During the experiments,

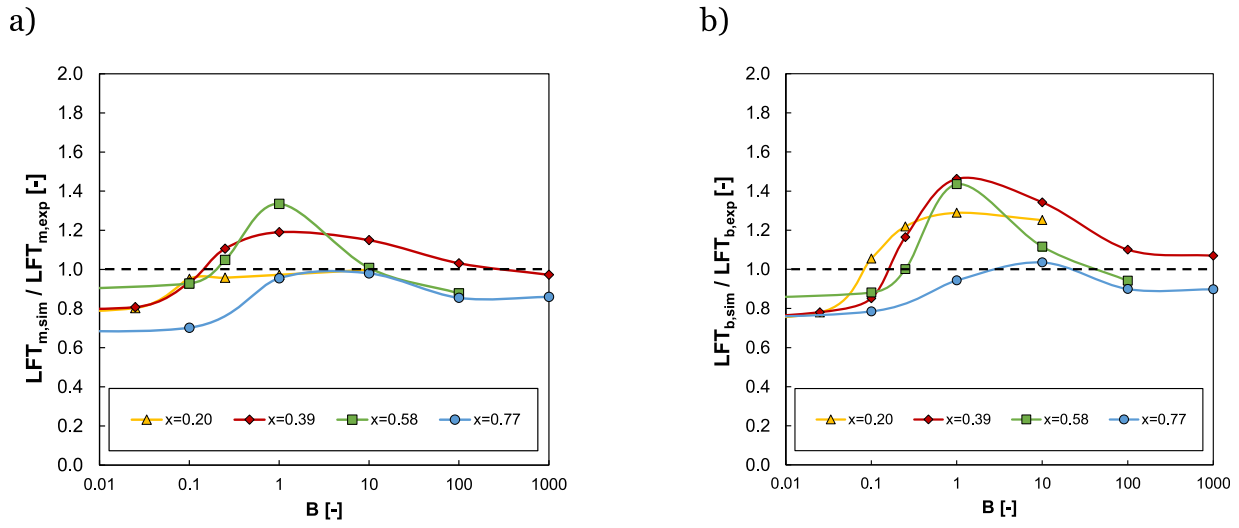

Fig. 7. Ratio between the simulated and the experimental values of a) mean and b) base liquid film thickness as a function of the damping parameter B. The results refer to R245fa at mass flux equal to 100 kg m^{-2} s^{-1}. Experiments are reported in Berto et al.[10].

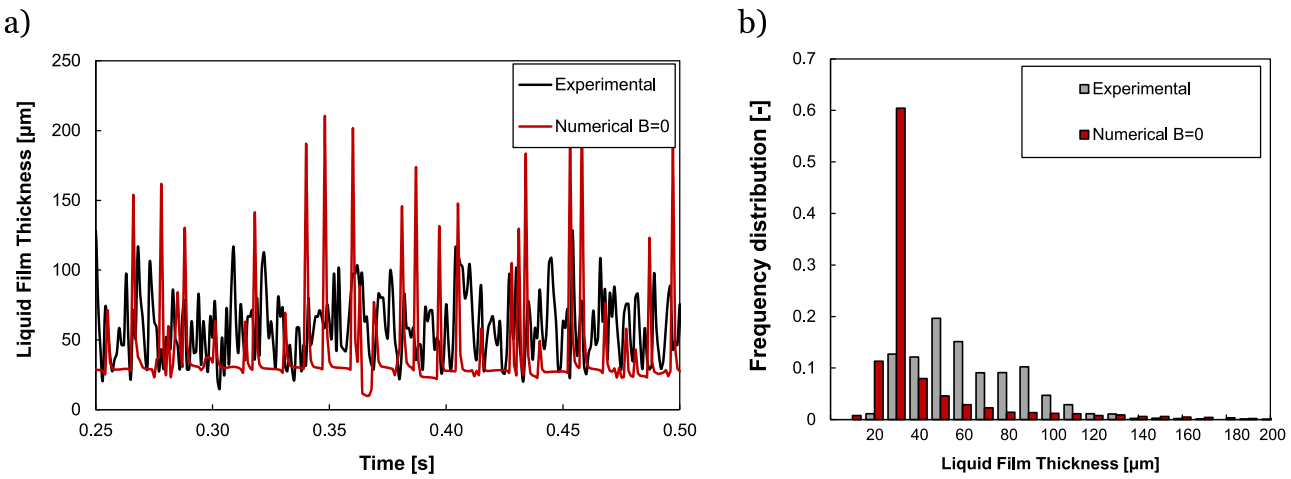

Fig. 8. Numerical results (with B=0) compared against experimental data for R245fa at G=100 kg m^{-2} s^{-1} and vapor quality x=0.77. a) Liquid film thickness (LFT) vs time. b) Frequency distribution of the liquid film thickness.

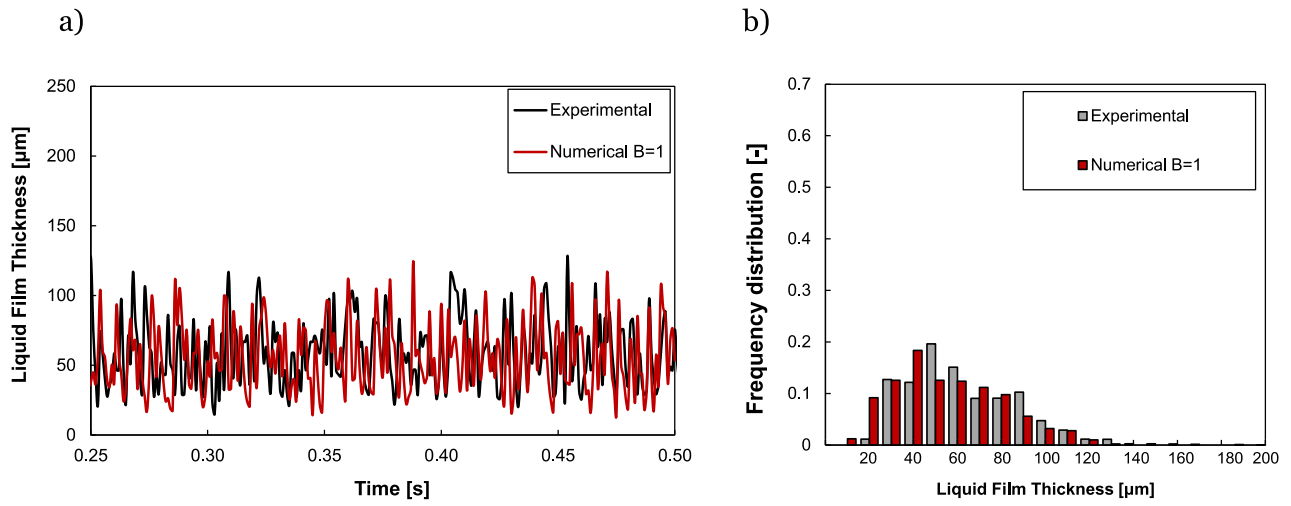

Fig. 9. Numerical results (with B=1) compared against experimental data for R245fa at G=100 kg m^{-2} s^{-1} and vapor quality x=0.77. a) Liquid film thickness (LFT) vs time. b) Frequency distribution of the liquid film thickness.

the chromatic confocal sensor is synchronized with the high-speed camera at 1000 Hz frequency to allow simultaneous liquid film thickness measurements and flow visualizations. Thanks to the synchronization, it is possible to obtain an in-situ calibration that links the apparent liquid film thickness (in pixels) resulting from the shadowgraph technique to the real liquid film thickness (in microns) measured by the confocal sensor. This calibration curve, which is valid up to the maximum measurable liquid film thickness of the confocal sensor (equal to 300 µm), can be extended by considering the theoretical calibration curve calculated from the ray-tracing model. The expanded standard uncertainty of the film thickness is ±2 µm in the case of the confocal sensor, while it varies between ±10 µm and ±15 µm when using the shadowgraph technique. More details regarding the optical system and the employed techniques can be found in Berto et al. [10,11].

5. Results

5.1. Numerical results vs experimental data of liquid film thickness

Numerical simulations have been performed with R245fa at mass flux G=100 kg m^{-2} s^{-1}, 40°C saturation temperature and vapor quality ranging between 0.20 and 0.77. The conditions for the simulations have been selected to be the same as the experimental tests. Table 2 reports a summary of the investigated conditions together with the measured and calculated values of mean/base liquid film thickness and void fraction ε. The void fraction is defined as:

$$\varepsilon = \left(1 - \frac{\mathrm{LFT}_m}{R}\right)^2 \tag{5.1}$$

First, the results without turbulence damping (B=0) are analysed. Looking at the void fraction, the relative deviation between numerical results and experimental data ranges between -0.9 % and -4.8 %. The CFD model accuracy is thus in line with that of the main void fraction correlations (see Berto et al. [11]). However, considering the liquid film thickness, larger deviations are encountered with the simulations systematically underpredicting the experimentally measured value: the relative error for the LFT_m and LFT_b are on average 20.9% and 24.1%, respectively.

To understand the reason for the deviation between calculated and measured liquid film thickness, turbulence damping at the interface has been considered by adding a source term in the ω equation (see Eq. (2.16) and Eq. (2.17)). In the present simulations, the B parameter has been varied between 0 (no turbulence dumping) and 1000. As reported in Section 1., considering the other works available in the literature dealing with numerical simulations of stratified or annular two-phase flows [21,26,29,30], the parameter B used to damp the turbulence

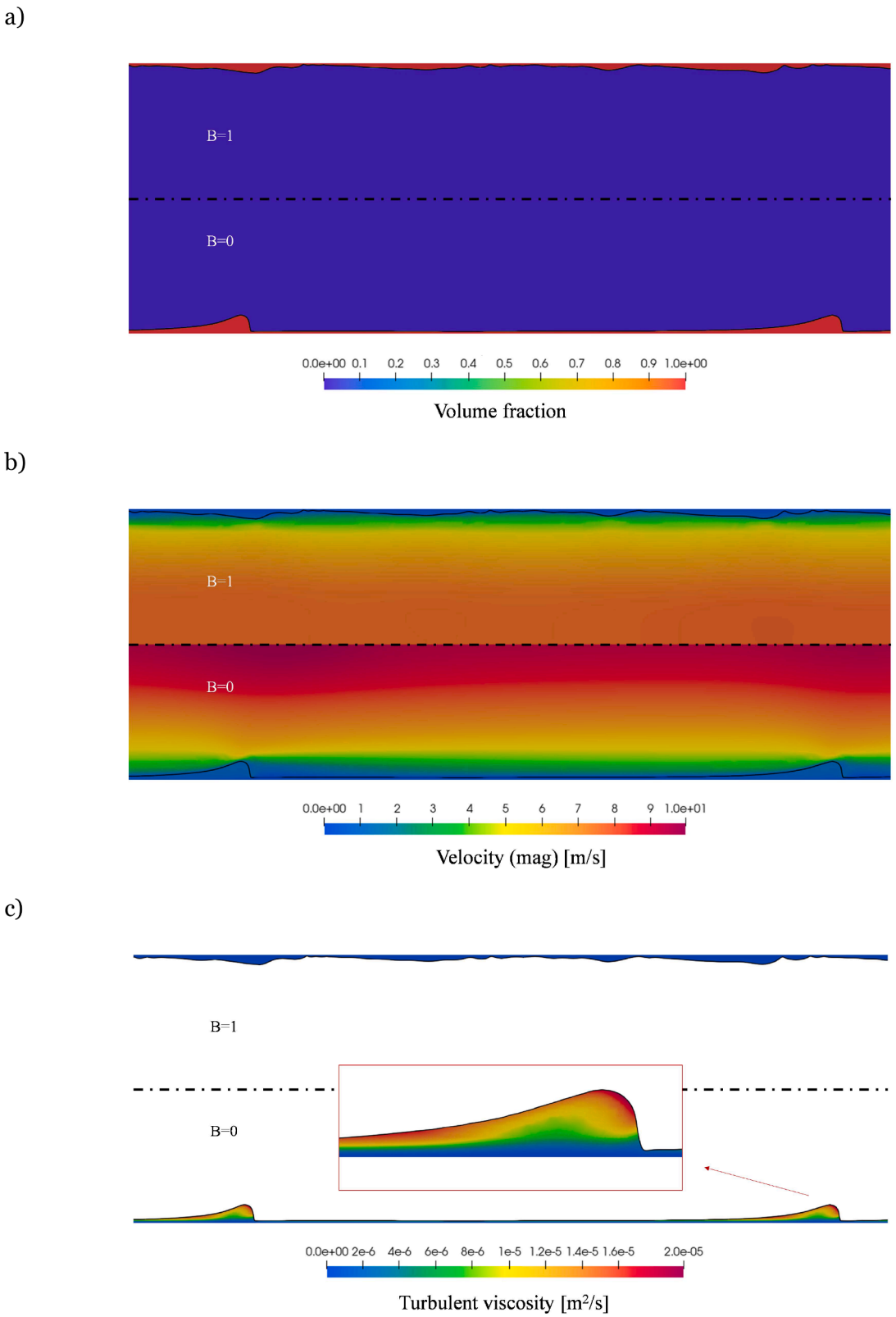

Fig. 10. Visualization of the main flow characteristics obtained from the simulations with R245fa at G=100 kg m^{-2} s^{-1} and vapor quality x=0.77. Results for B equal to 0 (lower half of the channel) and 1 (upper half of the channel): a) volume fraction, b) axial velocity magnitude c), kinematic turbulent viscosity in the liquid film.

ranges between 0 and 1000. Therefore, the range of variation for B used in the present work matches well to that reported in the literature. Fig. 7 reports the ratio between the mean and base liquid film thickness obtained by the simulations and the measured data as a function of B. The curves are reported in a logarithmic scale to allow clear visualization of the changes at low values of B. It can be observed that, as already mentioned, when the damping parameter B tends to zero, the average liquid film is always underpredicted by the numerical model. At

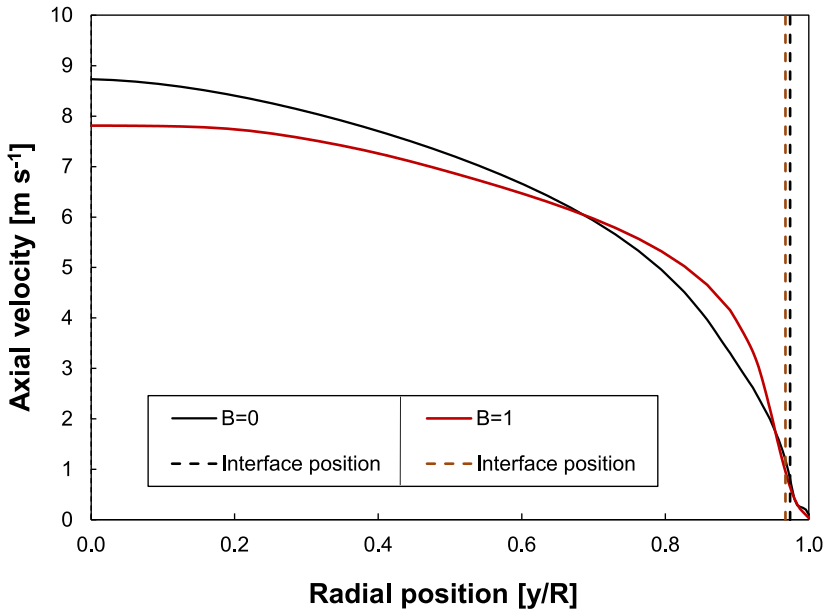

Fig. 11. Computed time-averaged axial velocity with R245fa at G=100 kg m^{-2} s^{-1} and vapor quality x=0.77 at x/L=0.9. Results for B equal to 0 and 1. The time-averaged interface position is also reported in the graph.

relatively low B values ($B \leq 1$), increasing B, the mean and base liquid film thickness tend to increase. For almost all the considered conditions, after a local maximum, the LFT_m and the LFT_b start to decrease tending to an asymptotic value. Hence, for each value of vapor quality, there is an optimal value of B which guarantees the best agreement with the experimental data. For x=0.20, the best agreement is found with B=10 for LFT_m and B=0.1 for LFT_b. For x=0.39, B=0.1-0.25 yields the best match for both LFT_m and LFT_b. Similarly, B=0.25 yields the best agreement for x=0.58. For x=0.77, a larger value of the coefficient, B=1-10, is required. Note that there is a general trend for the optimal value of B to increase with increasing the vapor quality and, thus, the mass flow rate of vapor.

An analysis of the results based only on void fraction and mean values of liquid film thickness does not provide information about the characteristics of the interfacial waves. A more detailed study is needed to understand the effect of turbulence dumping.

5.2. *Effect of turbulence damping on waves dynamics*

In order to better understand the effect of turbulence damping on interfacial waves, the measured and calculated liquid film thickness has been plotted vs time.

5.2.1. *Analysis for 0.77 vapor quality*

Fig. 8 a) reports the results obtained for vapor quality x=0.77 and parameter B equal to zero. Considering the numerical simulations, the liquid-vapor interface is characterized by a flat film (of about 30 μm thickness) with the appearance of regular disturbance waves. Instead, the vapor-liquid interface measured with the experiments is characterized by waves with higher frequency and smaller amplitude. This behavior can be confirmed by looking at the frequency distribution displayed in Fig. 8 b). The frequency distribution is obtained by dividing the whole range of variation for the LFT in intervals (bins) having the same size. Numerical results and experimental data are then sampled with a frequency equal to 1000 Hz. By counting the number of events that fall within each considered bin, the graphs in Fig. 8 b) can be realized. Considering the numerical results, the LFT interval characterized by the highest frequency is clearly identifiable; this is associated with the LFT of the flat film region. On the contrary, from the experiments, there are several LFT classes that display a relatively high frequency.

When considering the damping parameter B equal to 1, the average values of LFT_m and LFT_b obtained from the simulations are in good agreement with measurements (see Table 2). The temporal evolution and the statistical distribution of the liquid film thickness are reported in Fig. 9. It can be observed that when fixing B=1, the simulated frequency distribution matches the experimental one characterized by the presence of lower-amplitude ripple waves.

Fig. 10 a) reports the volume fraction field computed in a limited region of the domain, corresponding to x/L equal to 0.5, for two values of B (B=1 is shown in the upper half of the channel, B=0 in the lower half of the channel). It can be observed that the liquid zone is limited to the region close to the channel wall. The liquid film obtained considering the two values of B displays a substantially different behavior: in the case of B=0, two disturbance waves can clearly be recognized with no ripples between them (flat zone); in the case of B=1, the liquid-vapor interface is continuously rippled by small amplitude waves. Fig. 10 b) reports the field of the absolute velocity in the same part of the domain: as expected, the velocity in the liquid phase is much lower compared to that in the vapor phase. It can be observed that when the turbulence is damped at the interface (B=1), the velocity of the vapor phase at the center of the channel is lower compared to the case without damping (B=0). To better understand this effect, in Fig. 11 the profile of the time-averaged axial velocity is reported vs the radial position. It can be observed that the axial velocity and the axial velocity gradient in the vapor zone close to the interface are higher when considering B=1. In fact, the turbulence damping at the vapor side of the interface causes the turbulent viscosity to reduce and thus facilitates the flow in that region, which is less influenced by the slower liquid. However, since the vapor mass flow rate is imposed to be the same for both B values, the vapor velocity at the center of the channel with B=0 is higher.

Fig. 10 c) shows the turbulent kinematic viscosity in the liquid film. For B=0, a magnitude of the eddy viscosity up to 100 times larger than the molecular one (ν_l=2.5 × 10^{-7} m^2/s for saturated R245fa at 40 °C) is achieved in the correspondence of a wave. This is greatly reduced by setting B=1, which is the effect desired by the damping. Even if the asymmetric damping should have the effect of increasing the turbulence in the liquid, for B=1 the overall effect obtained is the damping of the turbulence everywhere, including the liquid (as clear when comparing B=0 and 1 in Fig. 10 c). This may not be true at higher B, as will be

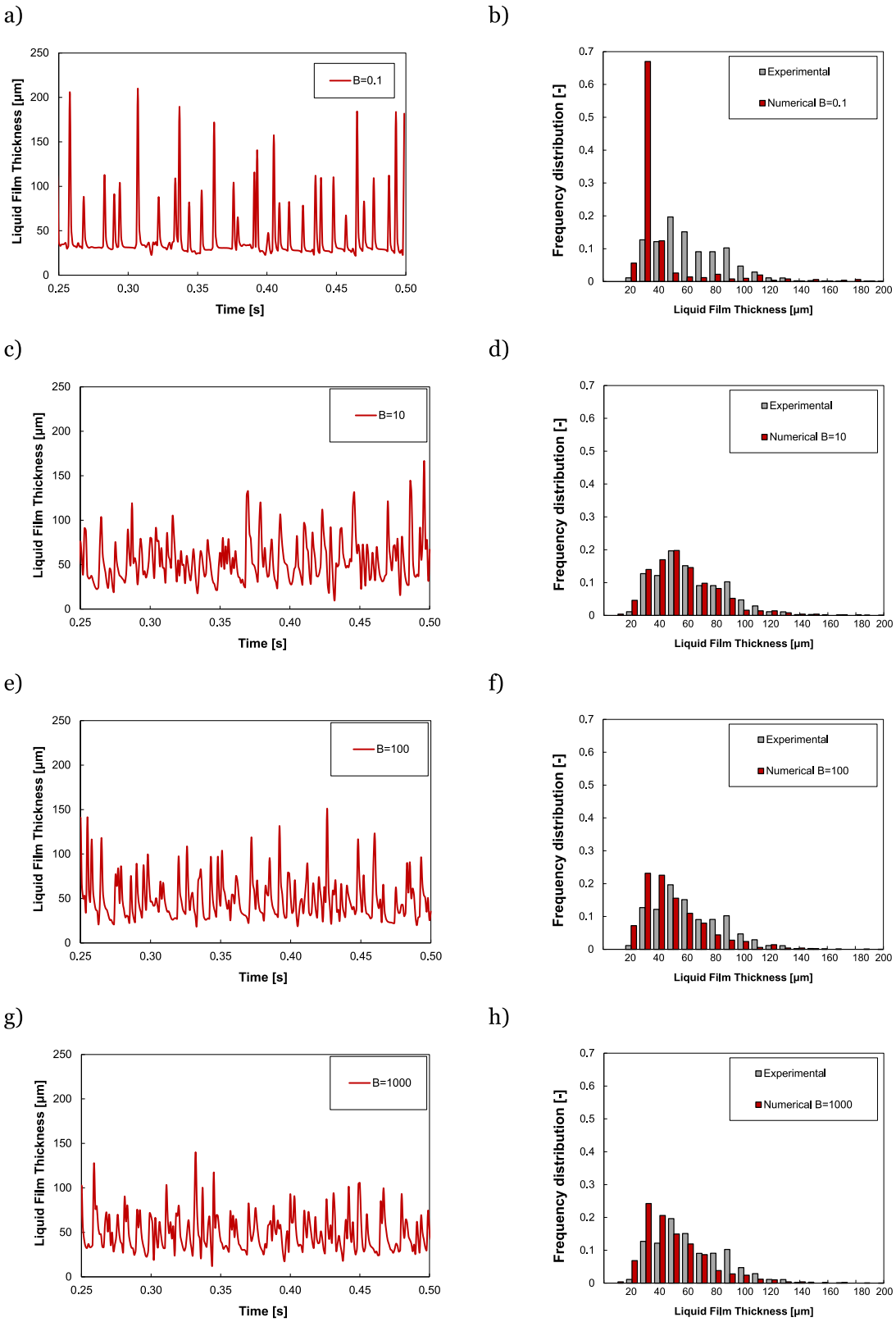

Fig. 12. Temporal evolution and frequency distribution of the liquid film thickness for the tests conducted with R245fa at G=100 kg m^{-2} s^{-1} and vapor quality x=0.77. Results for B between 0.1 and 1000.

discussed in Section 5.3.

Fig. 12 reports the temporal variation of the liquid film thickness and its probability distribution for other values of the damping parameter B. At B=0.1, the annular flow structure is similar to that found without damping the turbulence, displaying flat film regions between well-defined and regular disturbance waves; on the contrary, as B increases to values higher than 1, the waves display a much more chaotic trend, with many ripples appearing. The liquid film thickness achieved with

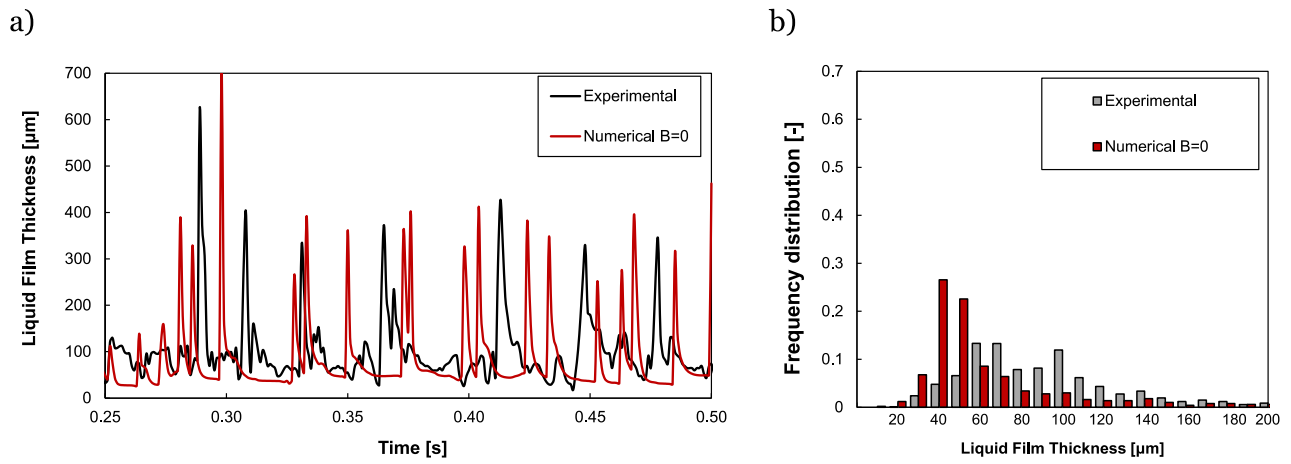

Fig. 13. Numerical results (with B=0) compared against experimental data for R245fa at G=100 kg m^{-2} s^{-1} and vapor quality x=0.39. a) Liquid film thickness (LFT) vs time. b) Frequency distribution of the liquid film thickness.

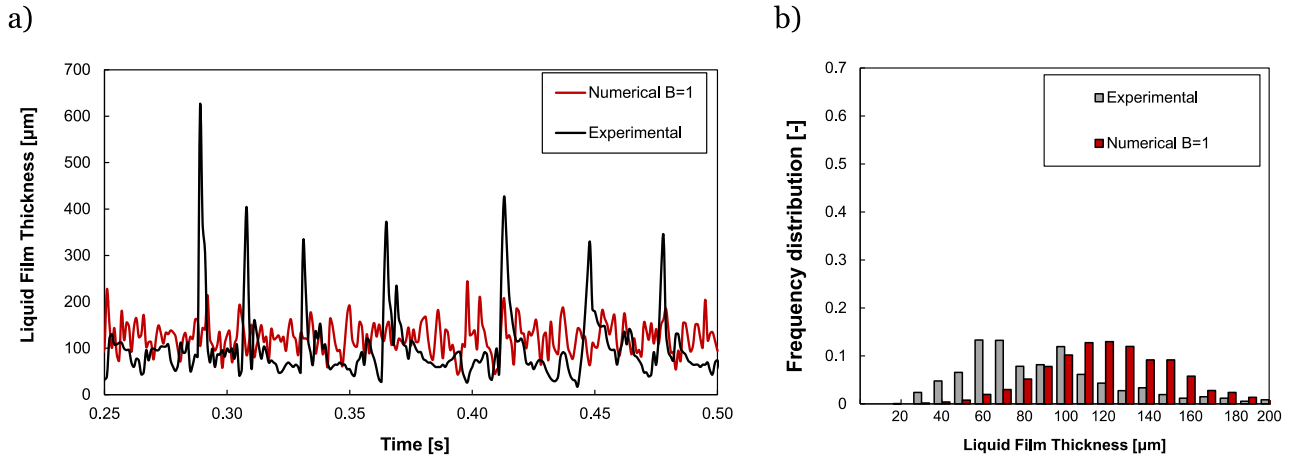

Fig. 14. Numerical results (with B=1) compared against experimental data for R245fa at G=100 kg m^{-2} s^{-1} and vapor quality x=0.39. a) Liquid film thickness (LFT) vs time. b) Frequency distribution of the liquid film thickness.

B=10 is similar to the one computed with B=1. However, the case B=10 seems to better capture the experimental wave frequency distribution in the range of thicknesses of 20–60 mm. By analysing the probability distributions, it can be also observed that at high values of B (equal to 100 and 1000), a wider range of higher probability LFT is encountered. A much more regular waves pattern is thus established in the latter cases. Furthermore, the values of LFT in the simulations at B=100 and 1000 decrease to below the experimental values, which is qualitatively similar to the results observed for small B.

5.2.2. *Analysis for 0.39 vapor quality*

The results obtained for a lower vapor quality, 0.39, are reported in Figs. 13 and 14 for the same reference cases of B=0 and B=1. Similar patterns to those observed for x=0.77 can be recognized for the instantaneous LFT: when no damping is performed, a flat film with high amplitude waves is detected; on the contrary, at B equal to 1 the film is thicker with much more chaotic and low amplitude ripples. However, the value of B=1 no longer yield the best agreement with the experiments, as the predicted liquid film is too thick and the frequency distribution shifted towards larger thicknesses.

Following the trend in Fig. 7 and the data in Table 2, the best agreement on LFT is achieved for B=0.1-0.25 and B=1000. The effect of the turbulence damping on the film thickness temporal evolution and probability distribution for other values of the damping parameter are displayed in Fig. 15. The results are reported for simulations realized with B equal to 0.1, 0.25, 100 and 1000. When B is equal to 0.1 the liquid film evolution is in agreement with the case without damping, displaying a flat film with regular appearance of disturbance waves. However, the amplitude of the disturbance waves is smaller. With a small increase in B, up to 0.25 and 1, the film is thicker on average but is mainly characterized by chaotic and low amplitude ripples. Therefore, B=0.25 provides a good estimation of the LFT but does not reproduce well the wave dynamics. On the contrary, when the damping parameter is further increased to 100 and 1000, high amplitude disturbance waves appear again together with small ripples and this is in line with the experimental flow characteristics. Likewise, the LFT is well predicted with these high values of B. Therefore, even if a good agreement in terms of average film thickness is achieved by both setting low and high values of B, the flow structure is better reproduced at B=100 and B=1000 (see and Fig. 15 f)-h)). It must be noted that this is valid for the test at vapor quality equal to 0.39, but it is not coherent with the outcomes at vapor quality equal to 0.77.

5.3. *Effect of the symmetric treatment*

As shown in Section 5.1, a small initial increase in the damping parameter B leads to an increase in the mean and base liquid film thickness until a local maximum is reached. The visualizations of the temporal evolution of the film thickness in Section 5.2 shows that, differently from the case in which no damping is applied, close to the

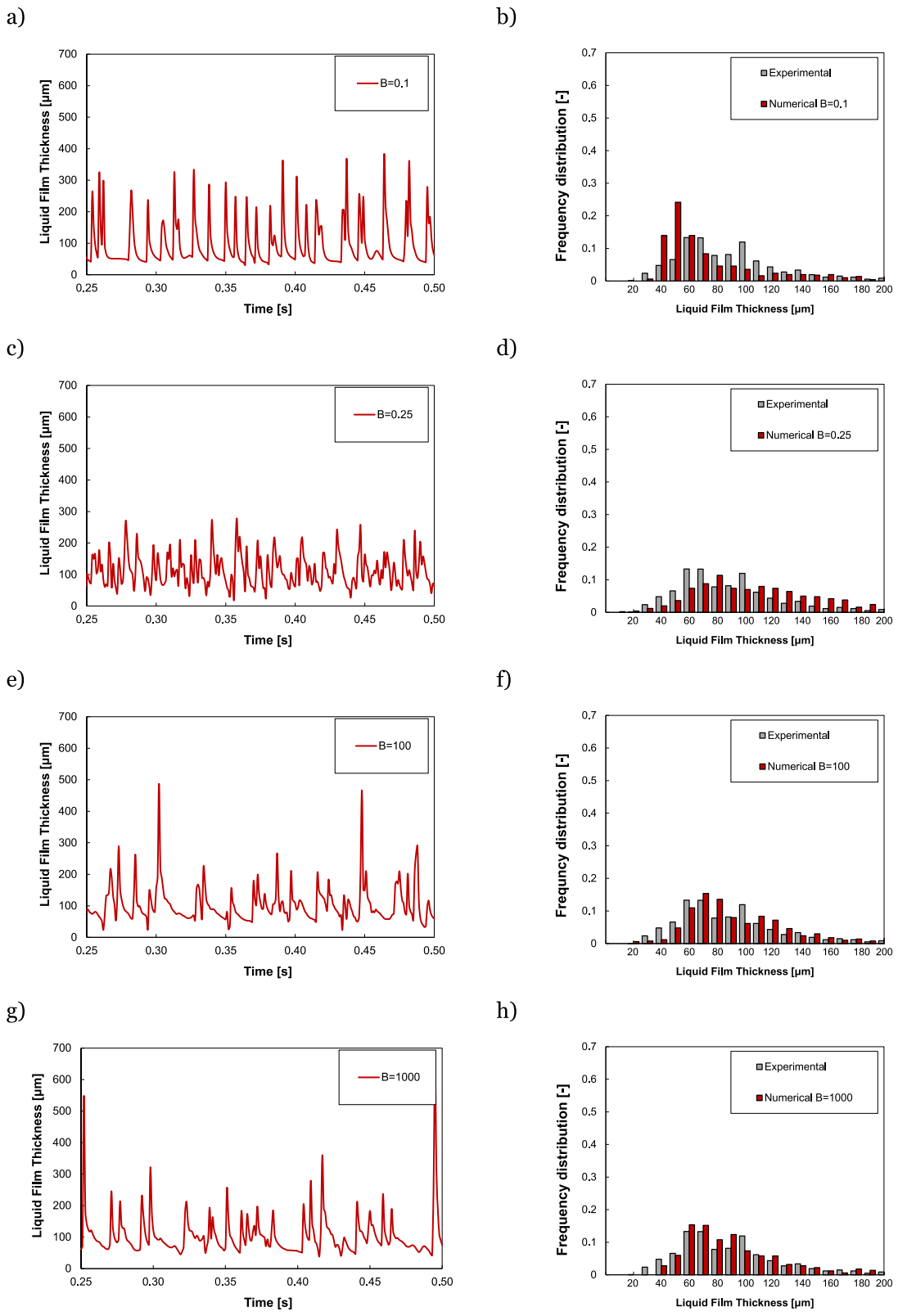

Fig. 15. Temporal evolution and frequency distribution of the liquid film thickness for the tests conducted with R245fa at G=100 kg m^{-2} s^{-1} and vapor quality x=0.39. Results for B between 0.1 and 1000.

mentioned maximum, there are no regular disturbance waves, and the liquid is mainly characterized by chaotic ripples (see Figs. 9 and 14). With a further increase in B, LFT$_m$ and LFT$_b$ decrease, and this is associated with the reappearance of high-amplitude disturbance waves, as can be clearly seen in Fig. 15 g). The reason for this non-monotonic behavior can be ascribed to the asymmetric nature of the ω source. As reported in Sec. 2.2, the damping source applied in the simulations presented above treats asymmetrically the two phases, by introducing

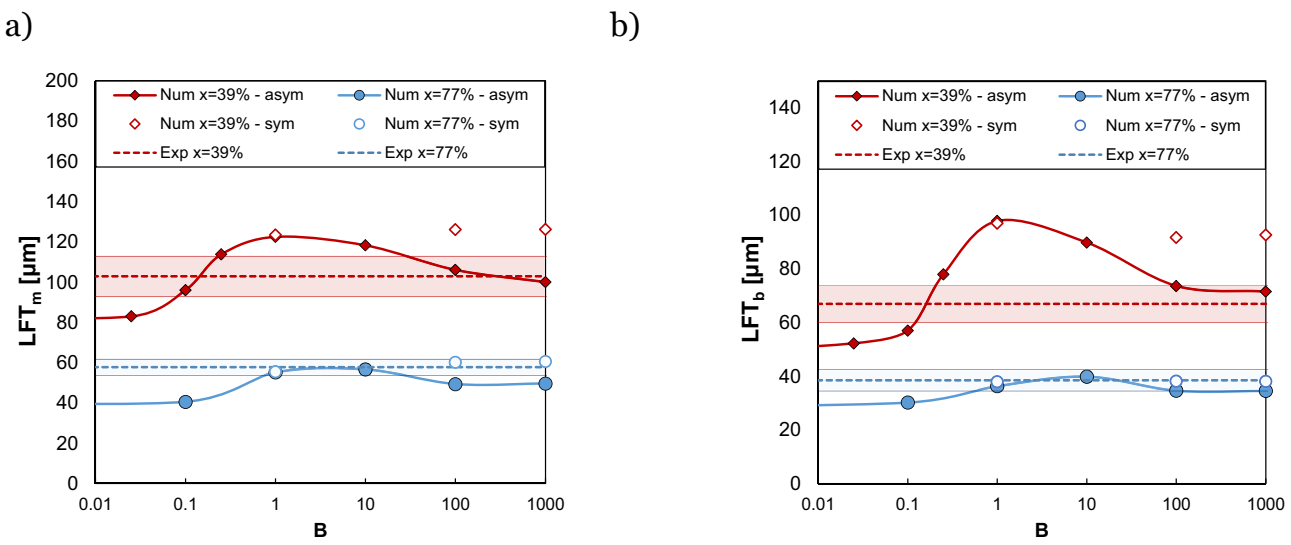

Fig. 16. Mean a) and base b) Liquid film thickness for the tests conducted with R245a at G=100 kg m^{-2} s^{-1} and vapor quality between 39 % and 77 %. The figures include both experimental data and the results obtained with asymmetric and symmetric treatment of the turbulence damping. The coloured region around the experimental value represents the expanded experimental uncertainty (coverage factor equal to 2) of the liquid film thickness.

the negative term δ_t, calculated according to Eq. (2.17), to the damping term on the liquid side of the interface. The effect of symmetric/asymmetric turbulence treatment across the interface has been rarely explored in the literature [44,45].

Fig. 16 reports the mean and base liquid film as a function of B for the tests at vapor quality equal to 0.39 and 0.77 obtained, both with an asymmetric (full symbols) and symmetric (void symbols) treatment. The symmetric treatment is obtained by setting δ_t=1 in Eq. (2.16), such that the damping source is positive in both phases. The result of this modification is the suppression of the turbulence both in the liquid and in the vapor side of the interface when B>0. According to Fig. 16, when the symmetric treatment is employed, the evolution of the mean and base liquid film thickness with the damping parameter is substantially different compared to the asymmetric case: for both the vapor qualities, an increase in B from 1 – 1000 does not lead to a significative variation in LFT$_m$ and LFT$_b$. This suggests that an asymptotic solution is reached for sufficiently high values of B, without intermediate maximum points for LFT. Furthermore, it is worth noticing that the asymptotic value of the mean and base liquid film thickness is approximately the same as the local maximum achieved with the asymmetric treatment. This can be seen in the simulations performed at vapor quality equal to 0.39: before decreasing to 106–100 μm for B>1, the maximum LFT$_m$ in the asymmetric simulations is equal to 123 μm, which is approximately the same value obtained at B equal to 1, 100 and 1000 with symmetric damping. This trend is qualitatively confirmed by the shape of the liquid film: this can be observed in Fig. 17, which reports the results obtained by setting the damping parameter at 0, 1 and 100. The pictures show the liquid contour and the kinetic turbulent viscosity field in the liquid phase obtained with both the symmetric and asymmetric treatment at the above-mentioned B values. It can be observed that the type of waves (mainly ripples) encountered at B=1, asymmetric, are comparable to those obtained in the simulations realized at the same or higher value of the damping parameter using the symmetric treatment (B=1 and B=100 symmetric). In these conditions, the turbulence is completely suppressed throughout all the liquid film (the turbulent viscosity is negligible). A different pattern is observed with the asymmetric simulation for B=100, where irregular high-amplitude disturbance waves appear, and whose peaks display highly enhanced turbulence. Also, the turbulent eddy viscosity in the liquid film is more than two orders of magnitudes higher than the molecular counterpart and about twice the value detected in the B=0 case, further emphasising that the asymmetric treatment at high B may actually increase the turbulence level in the liquid film. It is interesting to notice that, in the non-damped scenario (B=0 with the liquid film characterized by disturbance waves) the turbulent kinematic viscosity is notably higher than the one across almost all the interface, and not only in the correspondence of waves peaks.

6. Conclusions

The evolution of the liquid film during downward annular flow of refrigerant R245fa inside a 3.4 mm diameter circular channel is numerically investigated by using a geometric Volume of Fluid (VOF) method implemented in OpenFOAM open-source software. Simulations are run at 40 °C saturation temperature, mass flux equal to 100 kg m^{-2} s^{-1} and vapor quality ranging between 0.2 and 0.77.

A 2D axisymmetric domain is considered and Adaptive Mesh Refinement is applied to accurately reconstruct the interface. The turbulence is modelled with the k-ω SST approach and a source term is added in the ω equation to dump the turbulence near the vapor-liquid interface. The effect of turbulence damping is analysed by systematically varying the damping parameter B and the sign of the source term across the interface (symmetric and asymmetric treatment). Simulations results are compared against experimental data collected by using a chromatic confocal sensor and shadowgraph technique. The main results can be summarized as follows:

- For fixed values of vapor quality and mass flux, the computed liquid film thickness (LFT) at channel outlet is the same regardless of the vapor-to-liquid velocity ratio K assumed at the inlet of the computational domain.
- The computed thickness of the liquid film depends on the value of the damping parameter B. When the asymmetric treatment is applied, moving from a non-damped scenario (B=0) to B=1 leads to an increase of LFT$_m$ between 25 % and 52 %.
- The dynamic of the waves is influenced by the damping source term. For all the tested conditions, when B=0 the film is thin, flat and interspaced with regular and high-amplitude disturbance waves. On the other hand, when B=1 the film is characterized by low-amplitude chaotic ripple waves.
- Without turbulence dumping (B=0), numerical simulations underpredict the LFT. The computed LFT approaches the experimental

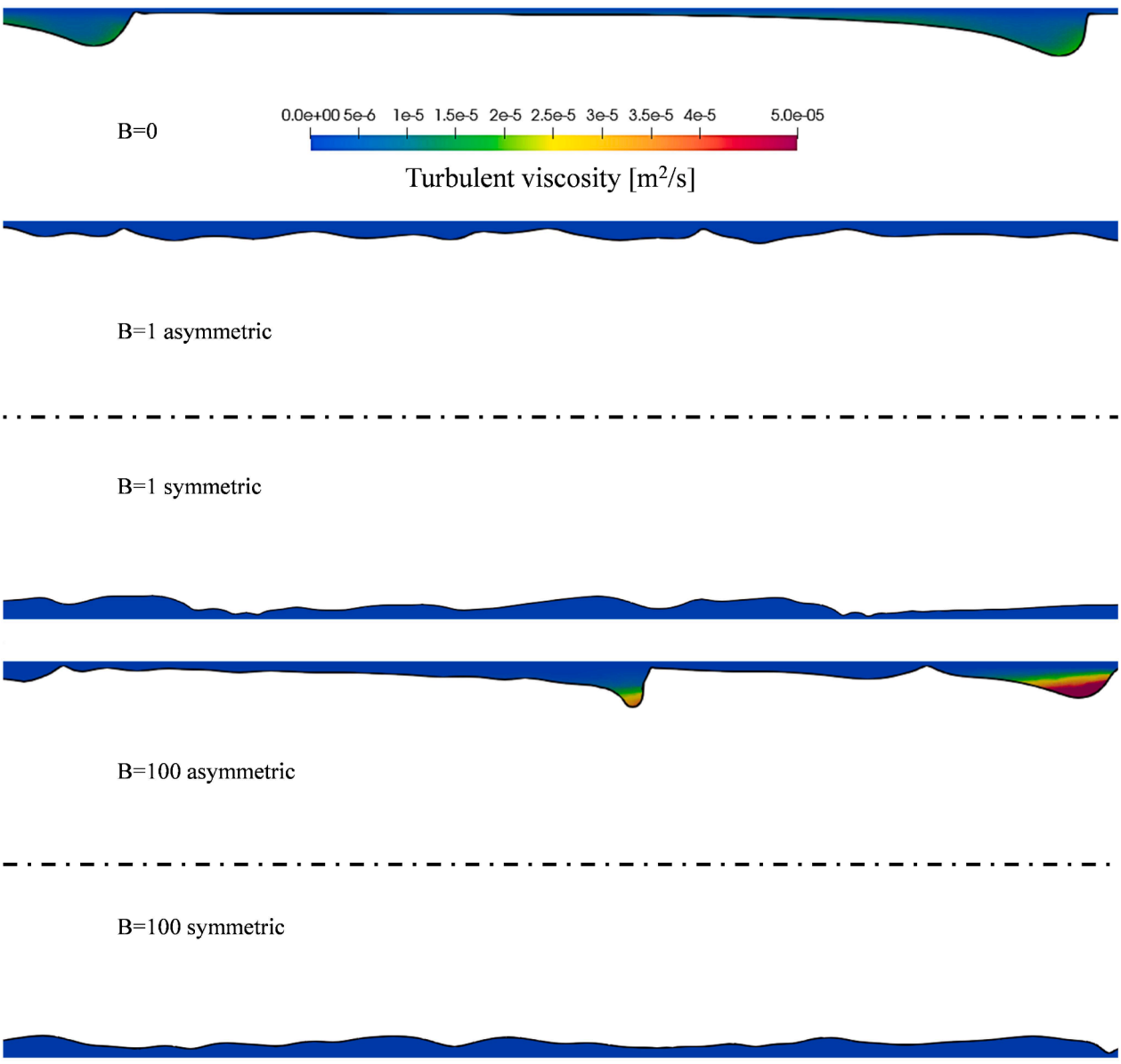

Fig. 17. Kinematic turbulent viscosity in the liquid obtained from the simulations with R245fa at G=100 kg m^{-2} s^{-1} and vapor quality x=0.39. Results for B equal to 0, 1 and 100 for both the symmetric and asymmetric treatment of the damping source.

values as B is increased, although this trend is not monotonic when an asymmetric damping approach is employed.

- For values of $B \leq 1$, the liquid film thickness and wave dynamics produced by the symmetric and asymmetric formulations are almost indistinguishable. When $B>1$, the symmetric treatment leads to a constant values of the LFT, whereas the asymmetric treatment results in a non-monotonic trend for the LFT with an enhancement of the turbulence in the liquid phase at high B.
- By varying the damping source term B between 0.1 and 1 it is possible to predict the experimental data with a mean absolute percentage error of 5 % for both the mean and base LFT and with a mean absolute percentage error lower than 1 % for the void fraction.

The optimum value of B capable of reproducing the experimental data has been found to be dependent on the operative conditions, therefore future analysis must be performed to extend the data set to other mass flow rates and other fluids. It must be mentioned that computational methods for the accurate prediction of the liquid film thickness are of practical interest in heat transfer applications. In fact, two-phase heat transfer processes (e.g. condensation, vaporization) take place often inside tubes and in annular flow regime. In particular, during annular flow condensation, the main thermal resistance is associated to the liquid film and it depends on liquid film thickness, turbulence and presence of interfacial waves. Adiabatic numerical simulations capable to track the vapor-liquid interface represent the first step for the development of future CFD tools for the design of two-phase heat exchangers.

CRediT authorship contribution statement

Emanuele Zanetti: Writing – original draft, Methodology, Formal analysis, Data curation, Conceptualization. **Arianna Berto:** Writing – original draft, Validation, Methodology, Investigation, Data curation. **Stefano Bortolin:** Writing – review & editing, Methodology, Funding acquisition, Conceptualization. **Mirco Magnini:** Writing – review & editing, Resources, Methodology, Funding acquisition, Conceptualization. **Davide Del Col:** Writing – review & editing, Supervision, Resources, Funding acquisition, Conceptualization.

Declaration of competing interest

The authors declare the following financial interests/personal relationships which may be considered as potential competing interests: Mirco Magnini reports financial support was provided by The Royal Society. Stefano Bortolin reports financial support was provided by Italian Ministry of Environment and Energy Security (MASE). If there are other authors, they declare that they have no known competing financial interests or personal relationships that could have appeared to influence the work reported in this paper.

Data availability

Data will be made available on request.

Acknowledgments

This work was supported by The Royal Society, grant number IES\R3 \203053. This work was also supported by MASE – ENEA program "Ricerca di Sistema Elettrico – Piano Triennale di Realizzazione PTR 2022–2024 – Tecnologie per la penetrazione efficiente del vettore elettrico negli usi finali". The contribution of Mr. Lorenzo Vianello is also gratefully acknowledged.

References

[1] H Han, Z Zhu, K Gabriel, A study on the effect of gas flow rate on the wave characteristics in two-phase gas–liquid annular flow, Nucl. Eng. Design 236 (2006) 2580–2588.
[2] RM Nedderman, CJ Shearer, The motion and frequency of large disturbance waves in annular two-phase flow of air-water mixtures, Chem. Eng. Sci. 18 (1963) 661–670.
[3] BJ Azzopardi, Disturbance wave frequencies, velocities and spacing in vertical annular two-phase flow, Nucl. Eng. Design 92 (1986) 121–133.
[4] KJ Chu, AE Dukler, Statistical characteristics of thin, wavy films: Part II. studies of the substrate and its wave structure, AIChE Journal 20 (1974) 695–706.
[5] KL Chu, AE Dukler, Statistical characteristics of thin, wavy films. III. structure of the large waves and their resistance to gas flow, AIChE 21 (1975) 583–593.
[6] RJ Belt, JMC Van't Westende, HM Prasser, LM Portela, Time and spatially resolved measurements of interfacial waves in vertical annular flow, Int. J. Multiph. Flow 36 (2010) 570–587.
[7] Y Zhao, CN Markides, OK Matar, GF Hewitt, Disturbance wave development in two-phase gas-liquid upwards vertical annular flow, Int. J. Multiph. Flow 55 (2013) 111–129.
[8] TA Moreira, RW Morse, KM Dressler, G Ribatski, A Berson, Liquid-film thickness and disturbance-wave characterization in a vertical, upward, two-phase annular flow of saturated R245fa inside a rectangular channel, Int. J. Multiph. Flow (2020).
[9] A Donniacuo, R Charnay, R Mastrullo, AW Mauro, Revellin R, Film thickness measurements for annular flow in minichannels: Description of the optical technique and experimental results, Exp. Therm. Fluid. Sci. 69 (2015) 73–85.
[10] A Berto, P Lavieille, M Azzolin, S Bortolin, M Miscevic, D Del Col, Liquid film thickness and heat transfer measurements during downflow condensation inside a small diameter tube, Int. J. Multiph. Flow 140 (2021) 103649.
[11] A Berto, P Lavieille, M Azzolin, S Bortolin, M Miscevic, D Del Col, Film thickness, interfacial waviness and heat transfer during downflow condensation of R134a, Appl. Therm. Eng. 214 (2022).
[12] A Berto, M Beaumale, P Lavieille, M Azzolin, S Bortolin, M Miscevic, D Del Col, Inter-laboratory optical measurements of film thickness during annular flow condensation in a small diameter channel, Exp. Therm. Fluid. Sci. 148 (2023) 110963.
[13] Y Zhang, L Jia, C Dang, Z Qi, Measurements of the liquid film thickness for annular flow during flow condensation in a circular tube, Int. J. Heat. Mass Transf. 187 (2022) 122552.
[14] W Fan, H Li, H Anglart, Numerical investigation of spatial and temporal structure of annular flow with disturbance waves, Int. J. Multiph. Flow 110 (2019) 256–272.
[15] BN Kishore, S Jayanti, A multidimensional model for annular gas–liquid flow, Chem. Eng. Sci. 59 (2004) 3577–3589.
[16] H Han, K Gabriel, A Numerical Study of Entrainment Mechanism in Axisymmetric Annular Gas-Liquid Flow, J. Fluids. Eng. 129 (2006) 293–301.
[17] Z Guo, DF Fletcher, BS Haynes, Numerical simulation of annular flow hydrodynamics in microchannels, Comput. Fluids. 133 (2016) 90–102.
[18] Z Guo, BS Haynes, DF Fletcher, Numerical simulation of annular flow boiling in microchannels, J. comput. multiph. flows 8 (2016) 61–82.
[19] H Li, MJBM Pourquié, G Ooms, RAWM Henkes, Simulation of a turbulent annulus with interfacial waves in core-annular pipe flow, Int. J. Multiph. Flow 154 (2022) 104152.
[20] H Li, MJBM Pourquie, G Ooms, RAWM Henkes, Simulation of turbulent horizontal oil-water core-annular flow with a low-Reynolds number k–ε model, Int. J. Multiph. Flow 142 (2021) 103744.
[21] N Varallo, R Mereu, G Besagni, CN Markides, Computational fluid dynamics modelling of the regular wave flow regime in air-water downwards annular flows, Chem. Eng. Res. Des. 201 (2024) 631–644.
[22] Y Liu, WZ Li, SL Quan, A self-standing two-fluid CFD model for vertical upward two-phase annular flow, Nucl. Eng. Des. 241 (2011) 1636–1642.
[23] M Fulgosi, D Lakehal, S Banerjee, V De Angelis, Direct numerical simulation of turbulence in a sheared air-water flow with a deformable interface, J. Fluid. Mech. 482 (2003) 319–345.
[24] Egorov Y, Boucker M, Martin A, Pigny S, Scheuerer M, Willemsen S, Validation of CFD codes with PTS-relevant test cases, *5th Euratom Framework Programme ECORA Project*, Vol. 2004, 2004, pp. 91–116.
[25] Menter FR, Zonal two equation k-w turbulence models for aerodynamic flows, 1993.
[26] W Fan, H Anglart, Progress in phenomenological modeling of turbulence damping around a two-phase interface, Fluids 4 (2019) 136.
[27] J Fabre, C Suzanne, L Masbernat, Experimental data set no. 7: stratified flow, part I: local structure, Multiph. Sci. Technol. 3 (1987) 285–301.
[28] P Porombka, T Höhne, Drag and turbulence modelling for free surface flows within the two-fluid Euler–Euler framework, Chem. Eng. Sci. 134 (2015) 348–359.
[29] Stäbler T, Experimentelle untersuchung und physikalische beschreibung der schichtenströmung in horizontalen Kanälen. 2007.
[30] VH Gada, MP Tandon, J Elias, R Vikulov, S Lo, A large scale interface multi-fluid model for simulating multiphase flows, Appl. Math. Model. 44 (2017) 189–204.
[31] W Fan, AV. Cherdantsev, H Anglart, Experimental and numerical study of formation and development of disturbance waves in annular gas-liquid flow, Energy 207 (2020) 118309.
[32] G Tryggvason, R Scardovelli, S Zaleski, Direct Numerical Simulations of Gas–Liquid Multiphase Flows, Cambridge University Press, Cambridge, 2011.
[33] JU Brackbill, DB Kothe, C Zemach, A continuum method for modeling surface tension, J. Comput. Phys. 100 (1992) 335–354.
[34] A Berto, M Azzolin, P Lavieille, A Glushchuk, P Queeckers, S Bortolin, CS Iorio, M Miscevic, D Del Col, Experimental investigation of liquid film thickness and heat transfer during condensation in microgravity, Int. J. Heat. Mass Transf. 199 (2022) 123467.
[35] E Da Riva, D Del Col, SV. Garimella, A Cavallini, The importance of turbulence during condensation in a horizontal circular minichannel, Int. J. Heat. Mass Transf. 55 (2012) 3470–3481.
[36] DC Wilcox, Reassessment of the scale-determining equation for advanced turbulence models, AIAA Journal 26 (1988) 1299–1310.
[37] J Roenby, H Bredmose, H Jasak, A computational method for sharp interface advection, R. Soc. Open. Sci. 3 (2016).
[38] A Mehdizadeh, SA Sherif, WE Lear, Numerical simulation of thermofluid characteristics of two-phase slug flow in microchannels, Int. J. Heat. Mass Transf. 54 (2011) 3457–3465.
[39] M Vermaak, J Potgieter, J Dirker, MA Moghimi, P Valluri, K Sefiane, JP Meyer, Experimental and numerical investigation of micro/mini channel flow-boiling heat transfer with non-uniform circumferential heat fluxes at different rotational orientations, Int. J. Heat. Mass Transf. 158 (2020) 119948.
[40] Joint Committee for Guides in Metrology (JCGM), Evaluation of measurement data - Guide to the expression of uncertainty in measurement, Bureau International Des Poids et Mesures (BIPM), Sèvres, France (2008).
[41] M Azzolin, S Bortolin, D Del Col, Convective condensation at low mass flux: Effect of turbulence and tube orientation on the heat transfer, Int. J. Heat. Mass Transf. 144 (2019) 118646.
[42] M Azzolin, A Berto, S Bortolin, D Del Col, Condensation heat transfer of R1234ze (E) and its A1 mixtures in small diameter channels, Int. J. Refrig. 137 (2022) 153–165.
[43] B Médéric, P Lavieille, M Miscevic, Void fraction invariance properties of condensation flow inside a capillary glass tube, Int. J. Multiph. Flow 31 (2005) 1049–1058.
[44] EMA Frederix, A Mathur, D Dovizio, BJ Geurts, EMJ Komen, Reynolds-averaged modeling of turbulence damping near a large-scale interface in two-phase flow, Nucl. Eng. Des. 333 (2018) 122–130.
[45] Z Dong, M Bürgler, B Hohermuth, DF Vetsch, Density-based turbulence damping at large-scale interface for Reynolds-averaged two-fluid models, Chem. Eng. Sci. 247 (2022) 116975.